Diagnosing cross-shelf transport along an ocean front: an observational case study in the Gulf of Lion

F. Nencioli,[1,2] **A. A. Petrenko,**[2] **A. M. Doglioli,**[2]

[1]Plymouth Marine Laboratory, Prospect Place, The Hoe, Plymouth, Devon, PL1 3DH, UK
[2]Aix Marseille Université, CNRS, Université de Toulon, IRD, MIO UM 110, 13288, Marseille, France

Key Points:

- Synergy between SST imagery, thermosalinograph and ADCP observations, and drifter trajectories
- Total along-front outflow from and inflow to the Gulf of Lion were 90 and 25 km^3 of water
- 3 to 4 of such events are sufficient for completely renewing surface waters in the Gulf of Lion

---

Corresponding author: Francesco Nencioli, `fne@pml.ac.uk`

Abstract

Exchanges between coastal regions and the open ocean are often associated with intermittent and localized processes such as eddies, fronts and filaments. Since these features are difficult to observe, their impact has been predominantly investigated using numerical models and remote sensing. In this study, satellite sea surface temperature maps, Lagrangian surface drifter trajectories, and ship-based surveys of currents and hydrography from the Latex10 campaign are used to quantify cross-shelf exchanges associated with a temperature front in the western Gulf of Lion. Satellite imagery and thermosalinograph sections provide the characterization of the various water masses associated with the front. Lagrangian drifter trajectories are used to identify the main transport structures and to quantify the velocity components associated with near-inertial oscillations. These are removed from the instantaneous ADCP observations with which the cross-shelf exchanges are then computed. The results indicate an average outflow of 0.074 ± 0.013 Sv and an inflow of 0.021 ± 0.006 Sv. Integrated over the two-week lifetime of the front, such outflow induced a total export of $\sim 90 \pm 14$ km^3 of water, indicating that 3 to 4 of such events are sufficient to completely renew the surface waters of the Gulf of Lion. The total import was $\sim 25 \pm 7$ km^3, suggesting larger inflows at depth or in the eastern part of the gulf to maintain its volume balance. These *in-situ* estimates represent a key term of comparison for the further development of numerical model- and satellite-based studies of cross-shelf exchanges associated with this type of processes.

1 Introduction

The coastal ocean is one of the most important and dynamic regions of the world [*UNESCO*, 2011]. It represents the main link between the continents, which are strongly impacted by human presence, and the open ocean, which is an important regulator of the global thermal and biogeochemical cycles. Furthermore, it provides a wide range of services and resources for human activities [*Barbier et al.*, 2011]. Along with river runoff and atmospheric forcings, exchanges with the open ocean at the continental shelf margin have been identified as one of the key factors controlling the environmental conditions of coastal regions [*Csanady*, 1982; *Huthnance*, 1995; *Liu et al.*, 2010]. Cross-shelf exchanges can regulate the fluxes of carbon [*Bauer and Druffel*, 1998; *Gattuso et al.*, 1998] and nutrients [*Grantham et al.*, 2004], as well as the dispersion of fish-larvae [*Roughan et al.*, 2006] and pollutants [*Gustafsson et al.*, 1998]. Therefore, they strongly influence the biogeochemical cycles and ecological conditions at both the local and global scale. Improving our understanding of the physical processes and mechanisms regulating such exchanges is, thus, a key step towards the development of a sustainable management of coastal environments [*EEA*, 2010; *UNESCO*, 2011].

In the last decades, cross-shelf exchanges have been the focus of several studies [e.g. *Brink and Cowles*, 1991; *Biscaye et al.*, 1994; *Huthnance et al.*, 2002; *Johnson and Chapman*, 2011]. However, accurate estimates of the net fluxes remain hard to obtain due to the temporal and spatial scales of the processes involved [*Huthnance et al.*, 2009]. Continental shelves are often bounded by strong large-scale (geostrophic) currents flowing along the steep bathymetry of the shelf edge [*Huthnance*, 1995]. These tend to inhibit cross shelf exchanges which, therefore, are mainly enabled by localized, short-lived and predominantly ageostrophic events, such as internal tide breaking [*Hopkins et al.*, 2012], Ekman transport [*Kirincich and Barth*, 2009], dense shelf water cascading [*Canals et al.*, 2006] and mesoscale-stirred fronts and filaments. The latter in particular have emerged in recent years as key contributors to ocean horizontal mixing and cross-shelf transport [*Nagai et al.*, 2015].

Due to their local and ephemeral nature, fronts and filaments remain an observational challenge [*Özgökmen et al.*, 2011]. *In-situ* observations from Lagrangian drifters [*Ohlmann et al.*, 2001; *Rubio et al.*, 2009] and gliders [*Castelao et al.*, 2008; *Heslop et al.*, 2012] have evidenced their importance in regulating the variability of cross-shelf exchanges. To extend the analyses to the regional and interannual scales, *in-situ* observations have often been integrated with numerical models [*Dinniman et al.*, 2003; *Juza et al.*, 2013; *Zhou et al.*, 2014] and satellite observations [*Matsuno et al.*, 2009; *Piola et al.*, 2010; *Shapiro et al.*, 2010]. At the same time, detailed *in-situ* characterizations of the dynamics and transport associated with specific events remain relatively rare [*Johnson and Chapman*, 2011]. Such observations can provide key information for further refining the accuracy of model- and satellite-based analyses, which in turn can be used to obtain more reliable estimates of cross-shelf exchanges where measurements are not dense enough [*Huthnance et al.*, 2009].

In this study, we use the observations from the Latex10 campaign (1-24 September, 2010) in the western Gulf of Lion (hereafter GoL) to provide (to the best of our knowledge) one of the first *in-situ* quantifications of the cross-shelf fluxes associated with a specific mesoscale-stirred front.

The GoL, located in the NW Mediterranean, is characterized by a large continental margin (Figure 1, top). The prominent feature of its circulation is the Northern Current (NC) a strong quasi-geostrophic current flowing from east to west along the continental slope [*Mil-*

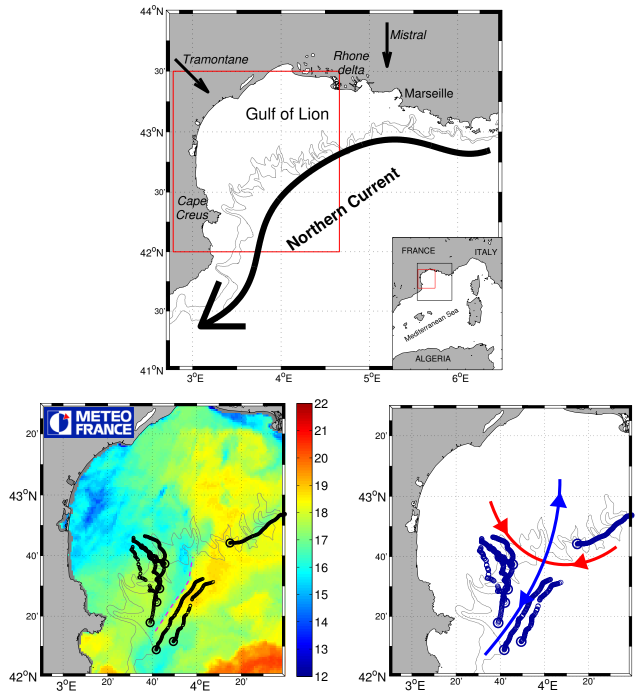

Figure 1. (top) Bathymetry of the Gulf of Lion. The 200 and 500 m isobaths mark the position of the continental slope (as in all following maps). Black arrows indicates the Northern Current, and the Tramontane and Mistral winds. The red rectangle indicates the region of focus of the Latex10 campaign. (bottom right) Drifter trajectories from 12 to 14 September 2010. Larger circles indicate the position of the drifters on 14 September 2010. In red and blue are the reconstructed repelling and attracting LCSs, respectively. (bottom left) Same drifter trajectories as in the right panel superimposed to AVHRR pseudo-SST (shaded) for 14 September [from *Nencioli et al.*, 2011]. The dashed line marks the front between colder GoL shelf waters and warmer open NW Mediterranean waters. After 14 September, the front moved to the west and extended further to the north, following the intrusion of the warmer open waters into the continental shelf (see Section 3.1).

lot, 1990]. The NC constitutes an effective dynamical barrier which blocks coastal waters over the continental shelf [*Albérola et al.*, 1995; *Sammari et al.*, 1995; *Petrenko*, 2003]. Exchanges with the open NW Mediterranean occur mainly through dense shelf water cascading [*de Madron et al.*, 2013] and NC instabilities, such as current meandering over the shelf and meso- to sub-mesoscale processes [*Estournel et al.*, 2003; *Petrenko et al.*, 2005, 2008; *Barrier et al.*, 2016]. (Sub)mesoscale eddies have been observed on both the eastern [*Allou et al.*, 2010; *Schaeffer et al.*, 2011] and the western part of the basin [*Hu et al.*, 2011a], where they play a major role in modulating the outflow from the continental shelf [*Kersalé et al.*, 2013]. Cross-shelf exchanges strongly influence the ecological conditions of the GoL, due to the strong biogeochemical gradients between coastal and open NW Mediterranean waters [*Malanotte Rizzoli et al.*, 2014; *Ross et al.*, 2016].

Latex10 was the third and last field campaign of the LAgrangian Transport EXperiment (LATEX, 2008-2011), which focused on the investigation of mesoscale-driven dynamics and cross-shelf exchanges in the western part of the GoL [*Hu et al.*, 2009, 2011a,b; *Campbell et al.*, 2013; *Kersalé et al.*, 2013]. The campaign included operations from two research vessels: the *R/V Le Téthys II* and the *R/V Le Suroît*. The Latex10 strategy was based on a novel adaptive sampling, which combined satellite altimetry, ship-based acoustic current Doppler profiler (ADCP) measurements, and iterative Lagrangian drifter releases, to collect repeated observations across a strong thermal front (Figure 1, bottom left). The dataset has already provided the rare opportunity to directly investigate and characterize some aspects of its dynamics: Lagrangian observation has been used to identify and track, for the first time, *in-situ* attracting and repelling Lagrangian coherent structures (LCS) associated with the front (bottom right panel of Figure 1) [*Nencioli et al.*, 2011]; furthermore, ship-based and Lagrangian observations have been combined together in a novel approach to compute *in-situ* estimates of submesoscale horizontal diffusivity across the front [*Nencioli et al.*, 2013].

In this study, we further integrate the ship-based (i.e. thermosalinograph and ADCP) and Lagrangian observations from Latex10 with remote sensing imagery (i.e. advanced very high resolution radiometer, AVHRR) to quantify the cross-shelf exchanges associated with the front. In particular: 1) the position of the *in-situ* LCS is used to identify the transport patterns in and out the western part of the GoL, and to select the ship tracks who crossed the front; 2) AVHRR imagery are combined with thermosalinograph observations from these cross-front sections to characterize the different water masses associated with the front; 3) Lagrangian drifter trajectories are used to track the water mass movements and to quantify the velocity components associated with near-inertial oscillations (NIO); 4) finally, the NIO components are removed from the instantaneous ADCP observations, and the corrected ADCP velocities are used to compute the cross-shelf exchanges resulting from the along-front advection of the identified water masses.

2 Data and Methods

2.1 Latex10 Observations

The hydrodynamical characteristics of the Latex10 front were surveyed by the *R/V Le Téthys II*. Measurements of surface temperature and salinity (hereafter SST and SSS, respectively) were collected every 15 seconds by a hull-mounted SeaBird SBE21 thermosalinograph at a depth of 2 m. Vertical sections of current velocities were collected by a hull-mounted VMBB-150 kHz ADCP. Following *Petrenko et al.* [2005], the instrument was configured for recording 1 minute ensemble averages with a vertical resolution of 4 m from 11 to 247 m of depth. At a cruise speed of eight knots, the thermosalinograph and ADCP sampling frequencies provided along-track spatial resolutions of 60 and 240 m, respectively.

Thermosalinograph observations were recorded continuously along the ship track from September 7 to September 24 except during profiling operations, when the thermosalinograph was turned off. ADCP velocities recorded during such operations were also discarded, since the accuracy of the measurements dropped significantly while the vessel maintained a fixed position. No measurements were collected on September 13, 16 and 19 due to rough sea conditions.

Wind speed and direction were recorded every 10 seconds by the meteorological station aboard the *R/V Le Suroît*. This second vessel was mainly used for the Latex10 passive tracer experiment, which consisted in the release and successive mapping of an SF6 patch in a Lagrangian reference frame [*Doglioli et al.*, 2013]. Due to its larger size (compared to the *R/V Le Téthys*), the *R/V Le Suroît* remained at sea for the whole duration of the campaign, providing a continuous time series of the meteorological conditions in the region of study.

Latex10 included the deployment of 14 Technocean Surface Velocity Program (SVP) subsurface drifters. Each drifter was tethered to a holey-sock drogue centered at 15 m depth, and equipped with a GPS transmitter which communicated its position every 30 minutes. The drifters were deployed in arrays of varying number, with initial separation distances between the drifters ranging from 3 to 5 km. Of the three array deployments performed during Latex10 [see *Nen-*

cioli et al., 2011, for more details], only the trajectories from the first two (hereafter Lyap01, launched on September 12, and Lyap02, launched on September 18) are analyzed in this study. In addition to those, 4 additional drifters with a drogue centered at 50 m were deployed in the eastern GoL at the beginning of the campaign. These were used exclusively to track the circulation along the GoL continental slope.

The analysis of *in-situ* observations was integrated with AVHRR channel 4 imagery (provided by Météo-France). Although AVHRR channel 4 (hereafter pseudo-SST) measurements are usually inaccurate in estimating the absolute values of SST, pseudo-SST imagery has shown to accurately identify the spatial distribution of SST gradients [see supporting information in *Nencioli et al.*, 2013]. SST gradients are particularly pronounced due to the contrast between GoL shelf (colder) and open NW Mediterranean (warmer) waters. This, along with its higher spatial (1 km) and temporal resolution (up to 4 images per day in the western part of the GoL), makes pseudo-SST imagery particularly suited for a qualitative analysis of the distribution, as well as the temporal evolution of mesoscale-driven dynamics along the continental slope of the GoL (bottom left panel of Figure 1). This was also evidenced during previous LATEX campaigns, when pseudo-SST images were used to investigate the dynamics of small mesoscale anticyclonic eddies in the western part of the GoL [e.g. *Hu et al.*, 2011a; *Kersalé et al.*, 2013].

2.2 LCS-based identification of cross-front transects

The reconstructed position of the *in-situ* LCS from *Nencioli et al.* [2011] has guided the identification of the cross-front transects within the time series of ship-based SST and SSS observations. A total of 12 cross-front transects were collected from 10 to 22 September (Table 1). These have been clustered together in four groups (hereafter A to D), each one including two or more passages over a similar region of the LCS within a time span no longer than 24 hours. For this reason, each group can be thought to be representative of a specific section of the LCS for a given day and, thus, is used to characterize its associated water masses and quantify their volume transport.

LCS and the associated hyperbolic points (the intersections of repelling and attracting structures) are powerful diagnostics for the investigation of ocean dynamics, as they provide direct information on transport and mixing patterns [*Haller and Yuan*, 2000; *d'Ovidio et al.*, 2004]. A water volume is stretched away from a repelling LCS while moving toward an hyperbolic point, whereas it is compressed toward an attracting LCS (which thus represent a trans-

Table 1. List of the 12 collected cross-front transects. The transects were clustered in 4 groups according to their location relative to the *in-situ* LCS and time of acquirement. The marks correspond to the ones used in Figures 2 and 4 to indicate the position of the beginning and end of each transect. Start and end time are expressed in local time (+2 GMT).

Group	Transect	Start Date	Time	End Date	Time	Marks
A	1	10 Sep	23:52	11 Sep	5:00	X-O
	2	11 Sep	5:04	11 Sep	10:13	O-X
B	1	14 Sep	12:56	14 Sep	18:32	X-O
	2	14 Sep	20:09	14 Sep	23:20	+-□
	3	15 Sep	2:41	15 Sep	5:25	O-□
C	1	17 Sep	9:06	17 Sep	14:13	X-O
	2	17 Sep	18:52	17 Sep	22:07	+-□
	3	17 Sep	22:12	18 Sep	1:25	□-+
D	1	20 Sep	18:18	20 Sep	20:53	X-O
	2	21 Sep	2:40	21 Sep	5:12	O-X
	3	21 Sep	5:30	21 Sep	7:47	X-O
	4	22 Sep	0:40	22 Sep	2:43	X-+

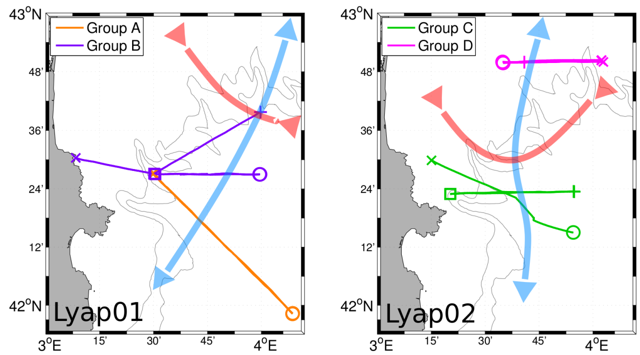

Figure 2. Position of the transects from the four groups in Table 1 and reconstructed *in-situ* LCS from *Nencioli et al.* [2011]. (Left) Transects from group A and B (orange and violet, respectively) and LCS from the Lyap01 drifter trajectories from 12 to 14 September. (Right) Transects from group C and D (green and magenta, respectively) and LCS from the Lyap02 drifter trajectories from 18 to 20 September. Because of the westward translation of the LCS, and the time difference between transect collection and LCS reconstruction, the relative position of the transects with respect of the LCS is only approximative.

port barrier) while moving away from an hyperbolic point [*Olascoaga et al.*, 2006; *Lehahn et al.*, 2007].

The *in-situ* LCS were reconstructed from the dispersion patterns of drifters arrays which moved from the GoL continental shelf to the open NW Mediterranean and vice-versa (bottom right panel of Figure 1). Therefore, they extended from inshore to offshore the continental slope, marking transport patterns of waters outflowing from and inflowing into the GoL. Since during Latex10 the flow was approximately horizontally non-divergent (see Section 3.1), the transport of a water volume along a LCS tangle was approximately conserved for different sections across the structures. On the basis of this assumption, it was possible to quantify the cross-shelf exchanges from and into the GoL from a series of transects across the attracting LCS, even if these were not collected along the GoL boundary (i.e. the continental slope; Figure 2). The attracting LCS were associated with the thermal front separating coastal from open NW Mediterranean waters. For this reason, the southern LCS was already identified by *Nencioli et al.* [2011] as the outer boundary of a corridor along which coastal waters escaped the GoL.

The south-western quadrant of the LCS tangle was characterized by the flow of GoL shelf waters that, after having moved eastward (along the western repelling LCS) towards the hyperbolic point at the outer-edge of the shelf-break, definitively escaped the GoL to the South (Figure 1). Thus, the first three groups of transects (A to C) collected across the southern attracting LCS east of Cape Creus from 10 to 17 September, have been used to estimate the outflow (i.e. southward flux) of GoL shelf waters associated with the front. On the other hand, the north-eastern quadrant was characterized by the flow of open sea waters that, after having moved westward along the outer edge of the continental slope (along the eastern repelling LCS), were deflected to the north as they approached the hyperbolic point, intruding into the continental shelf [see *Nencioli et al.*, 2011, for further details]. Thus, the transects of group D, collected along the northern attracting LCS, have been used to quantify the along-front inflow (i.e. northward flux) of open sea waters into the GoL.

2.3 Volume transport equation

Cross-shelf fluxes have been computed along the cross-front transects in Table 1 based on a discretized form of the volume transport equation. For a given transect tr, the volume transport VT_{tr} is defined by the integral

$$VT_{tr} = \int_{l_{ini}}^{l_{end}} \int_{z_{ini}}^{z_{end}} (\mathbf{u}_{tr}(l,z) \cdot \hat{\mathbf{n}}) \, \mathrm{d}l \, \mathrm{d}z \tag{1}$$

The unit vector $\hat{\mathbf{n}}$ defines the direction along which VT_{tr} is computed, so that l is the distance along the transect projected on the orthogonal direction to $\hat{\mathbf{n}}$; z is the depth; $\mathbf{u}_{tr}(l,z)$ is the horizontal velocity vector at a given distance and depth along the transect. In order to compute VT_{tr} from Equation 1, the direction $\hat{\mathbf{n}}$ and the integral limits l_{ini}, l_{end} (along-transect distance) and z_{ini}, z_{end} (depth) had to be defined.

The position of the *in-situ* LCS indicated an almost meridional orientation of the attracting structures (i.e. from NNE-SSW orientation for Lyap01 to N-S for Lyap02, Figure 2) [*Nencioli et al.*, 2013]. Because of that, $\hat{\mathbf{n}}$ was chosen as the unit vector pointing towards the North, so that cross-shelf fluxes have been computed along the north-south direction (potential errors associated with this choice are included in the error analysis in Appendix A). Following this orientation, l becomes the longitudinal distance and $\mathbf{u}_{tr}(l,z) \cdot \hat{\mathbf{n}}$ the meridional velocity component v_{tr} along each transect. Thus, positive and negative values of VT_{tr} indicate inflow to, and outflow from the GoL continental shelf, respectively.

It is important to remark that, to derive VT_{tr} based on ship-based ADCP velocities (as in this study), the observed values of v_{tr} cannot always be directly applied to equation 1. Ship-based ADCP velocities are an instantaneous measurement and, as such, they include the contribution of periodic motions such as tidal and near-inertial currents. Because of that, they are not always representative of the mean transport [*Petrenko et al.*, 2005]. In particular, observations collected when the periodic components are in(out of) phase with the mean background currents result in stronger(weaker) instantaneous velocities. In cases when the periodic motions are stronger than the mean background currents, the direction of the instantaneous velocities can even be opposite to the direction of the mean transport. Evaluating the presence and the magnitude of such motions, and removing their contribution from the instantaneous ADCP velocities, is therefore a key step for obtaining accurate estimates of cross-shelf exchanges from ship-based observations.

While the GoL is characterized by a weak tidal regime, NIO are a prominent feature of its dynamics: they are excited by the strong winds associated with the frequent events of Mistral or Tramontane and characterized by an inertial period of $\sim$ 17.5 h [*Millot and Crépon*, 1981]. Indeed, as shown by *Nencioli et al.* [2011], NIO were present in the western GoL during the Latex10 campaign. As described in more detail in Section 3.3, their magnitude has been retrieved from Lagrangian observations, and (when possible) their contribution removed from the instantaneous ADCP velocities. The resulting corrected meridional component $\tilde{v}_{tr}$ has been used in equation 1 to compute VT_{tr}.

As this analysis is based on observations within the first few tens of meters of the water column, the computed along-front cross-shelf exchanges correspond to the outflow of GoL shelf waters and the inflow of open NW Mediterranean ones within the upper mixed layer. Therefore, the along-transect integration limits l_{ini} and l_{end} were defined based on the presence of these surface waters along each transect (the identification and characterization of the different water masses are described in Section 3.2), while the depth integration limits z_{ini} and z_{end} were defined as the sea surface and the depth of the upper mixed layer, respectively. The lack of systematic cross-front vertical observations made it particularly challenging to accurately identify the variation of z_{end} along the various transects and for the different water masses. Nonetheless, 21 CTD casts were collected at various locations in the western GoL throughout the campaign (see supporting information Figure 1). Vertical profiles of temperature were used to estimate the mixed layer depth (hereafter MLD) at each cast. Following *de Boyer Montégut et al.* [2004], the MLD was defined as the depth at which temperature decreased by 0.2 °C with respect to the one at 10 m. Its average value was 22.8 m with a standard deviation of 4.8 m. Since the MLD variability did not show any strong temporal or spatial (i.e. distance of the CTD cast from the front axis) trends, z_{end} was set to the average MLD. The standard deviation was used in the error analysis in Appendix A.

Finally, the vertical integration of Equation 1 requires knowledge of the distribution of the corrected v_{tr} with depth. Observations from the first ADCP bin at 11 m revealed to be too noisy, and hence unreliable. Thus, on average, velocity measurements in the upper mixed layer are available at 15, 19 and 23 m depth. Because of this limitation, we decided to compute VT_{tr} by simply integrating from the sea surface to z_{end} the corrected meridional velocity component at 15 m depth $\tilde{v}_{tr,15}$. This is the same depth at which the drifter-based NIO used for correcting the instantaneous observations have been estimated. Furthermore, in doing so, we also implied that horizontal velocities were characterized by little vertical variations in the upper mixed layer. Direct comparison of the velocities observed between 15 and 23 m depth supported this assumption (see supporting information Figure 2).

Based on the above assumptions, Equation 1 was discretized as

$$VT_{tr} = \sum_{i=1}^{n} (VT_{tr})_i \tag{2}$$

where n is the number of along-transect observations associated with a given water mass and $(VT_{tr})_i$ the cross-shelf volume transport associated with a single velocity observation defined as

$$(VT_{tr})_i = (\tilde{v}_{tr,15})_i \, (\Delta l)_i \, \Delta z \tag{3}$$

where Δl is the distance (computed as central difference) between successive observations (at a cruise speed of $\sim$8 knots and with a frequency of acquisition of one measurement per minute, Δl is roughly 250 m along zonal sections); and Δz is the integration depth, set to a constant value of 25 m. Equation 2 has been used to estimate the along-front cross-shelf fluxes in Section 3.4.

3 Results

3.1 Origin and Characteristics of the Latex10 Front

The development of the Latex10 front have been characterized from the combined analysis of AVHRR pseudo-SST imagery and Lagrangian drifter trajectories. Figure 3 shows a sequence of successive maps of pseudo-SST from 29 August to 11 September. The map for 14 September is shown in Figure 1. Due to cloud coverage, no other images are available in the region during the Latex10 cruise. Available drifter trajectories within 1.5 days before and 1.5 days after the date of each image are superimposed to the pseudo-SST maps. The three drifters deployed before 3 September (indicated by squares in Figure 3) were tethered to 50 m drogues.

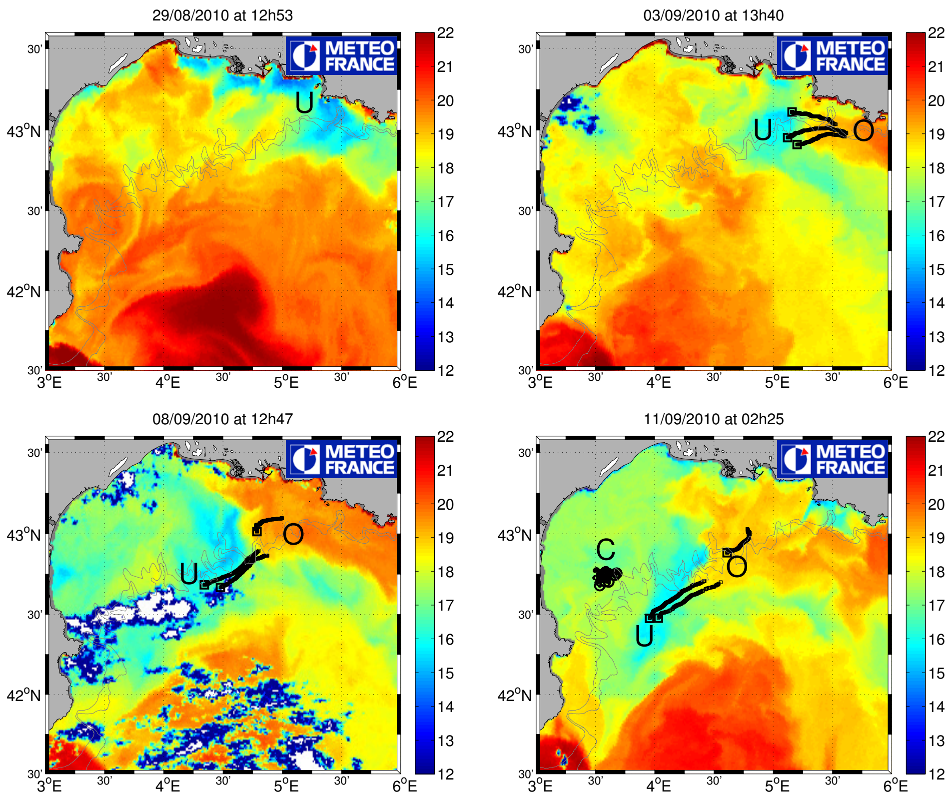

Figure 3. Successive maps of pseudo-SST. Superimposed in black are the drifter positions within 36 hours before and after each image was taken (reported on top of each plot). The buoys with 50 m drogues are indicated by squares, whereas the ones with 15 m drogues are indicated by circles (only present in the bottom right panel). U, C and O labels identify upwelled, continental-shelf and open NW Mediterranean waters, respectively. The larger squares/circles indicate the final positions of each drifter.

The nine drifters launched over the western part of the GoL continental shelf on 12 September (indicated by circles in Figures 1 and 3) were tethered to 15 m drogues. They correspond to the Lyap01 drifter array deployment.

The map of 29 August (Figure 3, top left) shows the presence of a series of patches of cold water along the eastern coastline of the GoL. During Latex10, no *in-situ* observations were collected in the eastern part of the GoL. However, given their location and the presence of strong Mistral conditions at the end of August 2010, these patches most likely originated from coastal upwelling, a common process for those areas [*Millot*, 1979]. For simplicity of notation, these upwelled waters from the eastern GoL are hereafter called “U waters”.

By the beginning of September, part of the U waters were displaced to the west by an intrusion of warmer open NW Mediterranean waters (hereafter "O waters") coming from the Ligurian basin, east of the GoL (Figure 3, top right). Within the following two weeks, both U and O waters were further advected to the west along the continental slope (Figure 3, bottom). The three 50 m drifters deployed at the eastern boundary of the GoL (black squares) show analogous along-slope trajectories, suggesting that the westward advection was not limited to the surface layer, but extended down to at least 50 m depth. The trajectories of the Lyap01 drifters indicate that, during the same weeks, waters in the western part of the continental shelf (colder than O waters but warmer than the U waters; hereafter "C waters") were advected southward, out of the GoL (Figure 1, bottom left). The convergence of the three different water masses (U, O and C) northeast of Cape Creus ($3°20'$E, $42°20'$N) led to the formation of the front observed during Latex10. After 14 September, the dispersion patterns of the Lyap02 drifter array (Figure 4, Groups C and D) indicate that the front axis migrated to the west and extended further to the north with respect to Figure 1, following the intrusion of O waters into the continental shelf.

The temporal evolution of the surface temperature (Figure 3) and the subsequent formation of the thermal front shown in Figure 1 is driven primarily by the horizontal advection of water masses with different temperature signatures. On the north-eastern side of the GoL, the temporal coherence between the drifters at 50 m and U waters at the surface suggests that the westward movement of U waters from Aug 29 - Sep 11 (Figure 3) was due primarily to advection by the nearly geostrophic NC along the slope [*Nencioli et al.*, 2013]. On the south-western side of the Gulf, the consistency between the southward motion of drifters at 15 m in C waters (Figures 1 and 3), and the modelled Ekman flow (see supporting information Figures 3 and 4) suggests that the southward movement of C water was due primarily to advection by the Ekman flow. In particular, two intense northeasterly wind events (discussed in Section 3.3) occurred during the first two weeks of September. For those events, the 15 m depth Ekman currents were reconstructed based on the winds from the weather-forecast model ALADIN provided by Météo-France ($0.1°$ spatial and 3-h temporal resolution [*Hu et al.*, 2009]) and the approach in *Liu et al.* [2014] (analogous results were obtained using the equations from *Ralph and Niiler* [1999], also applied to Lagrangian drifter analysis in *Lumpkin and Garzoli* [2005]). Thus, the front formation was mainly driven by the stirring induced by the interaction between wind-induced and large-scale (i.e. the NC) circulation [*Nencioli et al.*, 2013].

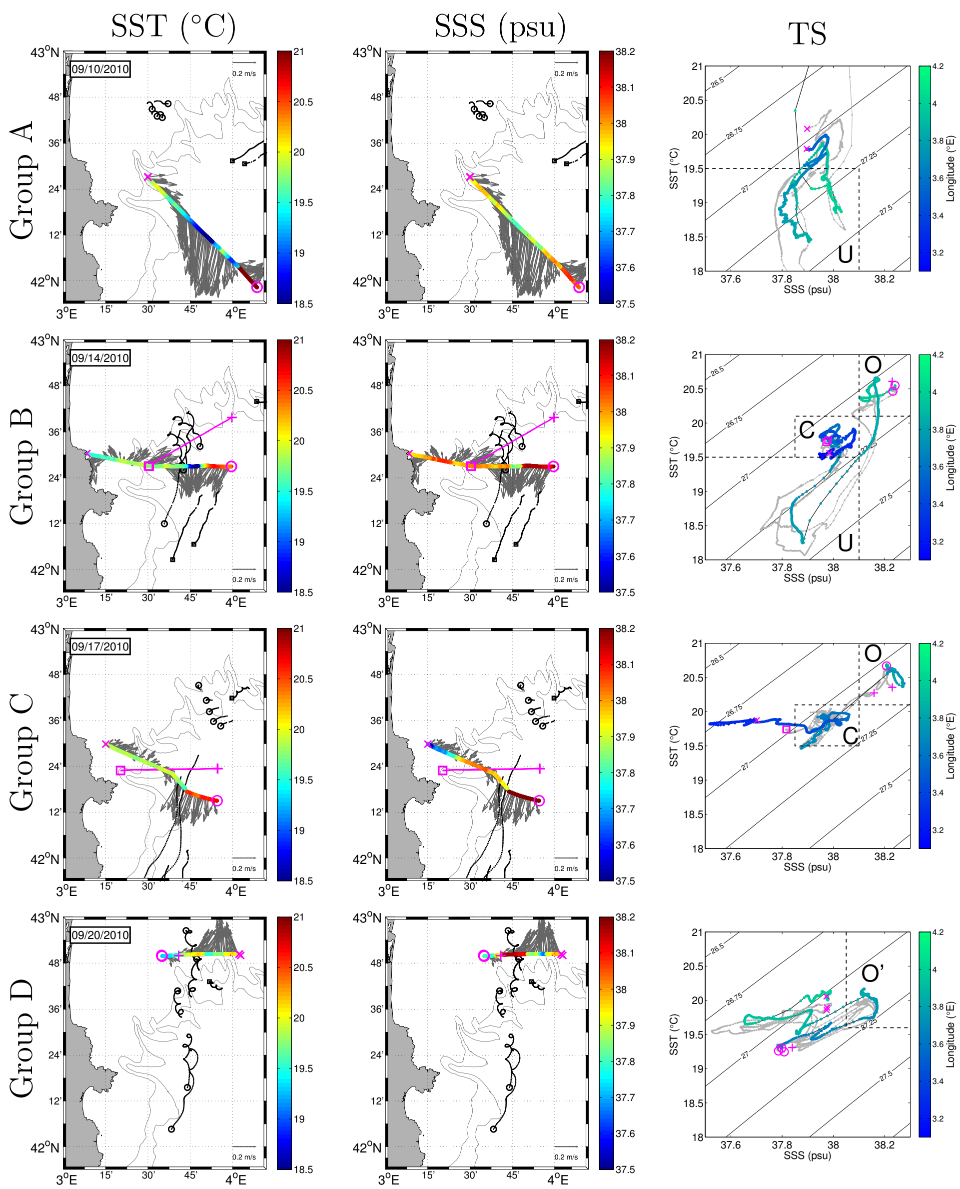

346 **Figure 4.** (Caption on the next page).

Figure 4. Hydrographical and dynamical characteristics of the four transect groups (A to D) used to compute cross-shelf exchanges from 9 to 21 September. Each row corresponds to a different group. (left column) Sea surface temperature recorded by the ship thermosalinograph (color), 15 m depth ADCP velocities (grey vectors) and drifter trajectories 24 hours before and after the transect was collected (black, as in Figure 3). For groups B and D, the velocity vectors are from the corrected velocities $\tilde{v}_{tr,15}$. In each figure, only the data from the first transect are shown. The positions of the other transects of the group are indicated in magenta. (center column) Same as left column but for sea surface salinity. (right column) TS diagram of the data from left and center columns. Each measurement is color coded according to its longitude to provide a reference of its location along the transect. Data collected from the other transects of the same group are shown in gray. Markers in magenta indicate the extremes of each transect, as in the figures in the center and left columns. The extremes of group A (top row) have SST values of $\sim 22.8°$C, above the axis limit, and thus are not shown. The gap in TS data in group C (third row) is due to ship operations (i.e. CTD profiling) during which the thermosalinograph was turned off (see also Figure 10). The dotted lines indicate the temperature and salinity limits that identify the upwelled (U), the continental shelf (C) and the open NW Mediterranean (O) waters. The limits of open waters (O') in group D (fourth row) are adjusted to lower values due to a general decrease in SST and SSS induced by a storm event affecting the entire western part of the GoL between 18 and 19 September. The same limits were used in Figures 8 to 11 to identify regions of inflow and outflow of those waters across the various transects and to derive the cross-shelf exchanges.

The horizontal circulation associated with the front was characterized by the southward flow of U and C waters and the northward flow of O waters. Both U and C waters originated within the GoL (in the eastern and western part, respectively). By moving south along the front, they permanently escaped the GoL towards the Catalan basin. Therefore, their southward flow corresponds to the outflow of shelf waters from the GoL discussed in Section 2.2. On the other hand, the northward intrusion of O waters (originated from the Ligurian basin) northeast of Cape Creus corresponds to the inflow of open sea waters into the GoL. These represented the two main contributions to the cross-shelf exchanges associated with the front that were observed and quantified during Latex10.

Analysis of the thermohaline characteristics of the front evidences that for Groups A and B the cross-front transitions between the different water masses were characterized by density gradients (see the T-S plots in Figure 4 and supporting information Figure 5). In particular, the gradients were quite sharp between U and outer shelf waters (> 0.4 kg m^{-3} per 4 km) but slightly less pronounced between U and continental shelf waters (~ 0.2 kg m^{-3} per 8 km). On the other hand, for Groups C and D, when only C and O waters were observed in the sections, the front became mostly compensated: the horizontal gradient of temperature was balanced by the salinity gradient, so that the resulting cross-front density profile was almost constant. The distribution of the vorticity Rossby number ($\mathrm{R}_0 = \zeta/f$, with ζ the vertical component of relative vorticity and f the Coriolis parameter) computed along the cross-front transects shows predominant values smaller than $\mathcal{O}(1)$, with occasional maxima around $\mathcal{O}(1)$ (see supporting information Figure 6). As in *Klymak et al.* [2016], ζ was assumed to be dominated by the contribution of the cross-front gradient of the along-front velocity. Following *Shcherbina et al.* [2013], the along-front spatial derivatives were computed at a given point as the slope of the linear function fitted to the velocity observations within a certain searching radius around the point. The searching radius was set to 800 m, so that 7 points were usually used for the fitting.

Although the Latex10 front may have been associated with a surface intensified geostrophic flow and stronger vertical velocities where the horizontal density gradient and relative vertical vorticity were large, we do not explicitly explore the role of the local frontal dynamics [e.g. *Thomas et al.*, 2008] in driving the cross-shelf exchange in this manuscript. Instead, we use the thermohaline gradient associated with the front as a diagnostic indicator of the spatio-temporal structure of the larger scale and largely horizontal geostrophic and Ekman flows that form the front. The implicit assumption is that the horizontal advection by these large scale flows is driving the temporal evolution of surface temperature [*Nencioli et al.*, 2013] as well as the cross shelf exchange that we observe, and that the local frontal dynamics is not crucial to the evolution of either of the two. An exploration of this hypothesis is beyond the scope of the present work and probably beyond the reach of these particular observations.

3.2 T-S Signature of the Exchanged Waters

In this section, the SST and SSS signature of U, C and O water masses are defined through the combined analysis of AVHRR pseudo-SST imagery, Lagrangian drifter trajectories and ship-based *in-situ* observations. Pseudo-SST provides the relative temperature signature of the different masses, and the drifter trajectories indicate their horizontal movement. Both sets of measurements are used to identify the presence of the water masses along each group of transect. Within each thermosalinograph sections, U, C and O waters are characterized by clusters of observations around specific T-S values (Figure 4 right column and supporting information Figure 7). These are separated by relatively sharp gradients The thresholds identifying the different water masses are defined along those gradients. Although such definitions are somehow arbitrary, the final results of our analysis do not show significant sensitivity to these choices (see discussion on l_{ini} and l_{end} in Appendix A).

ADCP and thermosalinograph SST and SSS for the four groups of transects are shown in Figure 4 (A to D from top to bottom row, respectively). ADCP velocities for the first three groups (A to C) indicate the presence of relatively strong southward currents (> 0.3 m s^{-1}) immediately offshore the continental shelf in front of Cape Creus. Drifter trajectories are consistent with the ADCP observations, indicating that the transects crossed the southward flow of U and C waters. Thus thermosalinograph observations from groups A to C have provided their temperature and salinity thresholds.

Group A (Figure 4, top row) includes two transects collected back and forth along the same track between 10 and 11 September. As also indicated by pseudo-SST imagery (Figure 3, bottom left), the colder and less saline waters (between 3°40'E and 4°E) associated with the southward flow correspond to U waters. The observations indicate that they were characterized by temperature $<$ 19.5°C and salinity $<$ 38.1 psu (group A TS plot in Figure 4). To the southeast, U waters are bounded by much warmer and saltier waters (∼22.8°C, ∼38.1 psu; because of that, the southeastern extreme of the transect is above the upper limit of the y-axis of the TS diagram). These occupied most of the central NW Mediterranean on late summer 2010 (Figure 3, bottom left).

Group B (Figure 4, second row) includes three transects collected between 14 and 15 September. As opposed to group A, the transects were not all performed along the same tracks. Nonetheless, as evidenced by the TS digram for group B in Figure 4 they all show similar hydrographical and dynamical characteristics (see also Section 3.4), further supporting the clustering adopted in Section 2.2. Like in group A, the southward flow region is still characterized by the presence of U waters with temperature $<$ 19.5°C and salinity $<$ 38.1 psu (between 3°45'E and 3°50'E). As indicated by the Lyap01 drifter trajectories (black circles), U waters are bounded to the West by warmer and saltier waters flowing southward off the continental shelf. These correspond to C waters, characterized by temperature between 19.5 and 20.1°C, and salinity between 37.85 and 38.1 psu (group B TS plot in Figure 4). The C waters are found along the whole western part of the transect, from offshore the continental slope to the coast north of Cape Creus. On the eastern side of the transect, U waters are still bounded by warmer and saltier waters. However, these are colder and slightly saltier than the waters found east of the front in group A. Trajectories of the 50 m drifters (black squares) suggest that they correspond to the O waters advected from the eastern GoL by the NC. Thus, O waters were characterized by temperature $> 20.1°$C and salinity > 38.1 psu (Group B TS plot in Figure 4). This distribution of water masses along the transects of group B is consistent with the pseudo-SST imagery for the same day (Figure 1, bottom left).

Group C (Figure 4, third row) includes three transects collected between 17 and 18 September along tracks similar to the ones of group B followed a few days before. The five drifter trajectories across the continental slope northeast of Cape Creus (black circles) correspond to the Lyap02 array deployed on 18 September. Thermosalinograph observations indicate the absence of U waters along the transects. Therefore, the front was characterized by the direct transition from C waters (between 3°30'E and 3°43'E) to O waters (east of 3°43'E). The western part of the transect evidences a gradual transition from C waters to less saline waters ($<$ 37.85 psu) over the continental shelf [referred to as littoral waters, L, in *Nencioli et al.*, 2013].

Group D (Figure 4, bottom row) includes four zonal transects over the continental shelf at $42°50'$N. These were collected between 20 and 22 September. Drifters trajectories show that between 18 and 22 September three of the Lyap02 drifters were advected from south to north into the GoL. Ship-based SST and SSS observations confirm that those trajectories are associated with the shelf intrusion of warmer and saltier O waters from the continental slope (between $3°40'$E and $3°50'$E). The TS plot for group D in Figure 4 evidences the presence of these waters in all four transects of group D. However, their signature is characterized by lower T-S values than in groups B and C. This is consistent with what *Nencioli et al.* [2013] reported; they observed a decrease in both temperature (∼0.5°C) and salinity (∼0.05 psu) of O waters after 20 September, due to strong wind and intense rain conditions in the western part of the GoL between 18 and 19 September. Because of such modifications, the intruding waters are re-labelled O' and their temperature and salinity thresholds lowered to $> 19.6°$C and > 38.05 psu, respectively. Other water masses were present over the continental shelf on September 20. However, due to the lack of cloud-free pseudo-SST imagery and drifter trajectories in the western part of the continental shelf, their origin and contribution to the cross-shelf exchanges cannot be reliably evaluated.

The identified SST and SSS thresholds for the three water masses will be used in Section 3.4 to define the integration limits l_{ini} and l_{end} from equation 2. Observations from groups

A to C will be then used to quantify the southward fluxes of U and C waters, while observations from group D to quantify the northward flux of O waters.

3.3 Near-Inertial Oscillations

As already discussed in Section 2.3, the western part of the GoL was characterized by strong NIO at the time of the Latex10 campaign. Because of that, our analysis included corrections to remove the contribution of their components from the instantaneous ADCP observations in order to obtain more reliable estimates of cross-shelf fluxes from equation 2.

A first indication of NIO can be inferred by the anti-cyclonic (i.e. clockwise) spirals characterizing the Lyap01 and Lyap02 drifter trajectories in Figure 4 (panels from groups B and D, respectively). Along-track ADCP observations also indicate their presence. However quantifying the magnitude of NIO velocity components directly from those measurements is particularly challenging. Ship-based observations include both spatial and temporal variability and the two are often hard to untangle. Some methods have been proposed in the past to separate the NIO components from the signal of large-scale circulation [e.g. *Chereskin et al.*, 1989; *Garcia Gorriz et al.*, 2003; *Petrenko et al.*, 2008]. However, they cannot be reliably applied to the Latex10 observations, since they focused on processes characterized by shorter and faster scales of variability. For instance, the shorter transects (in both space and time) compared to studies focusing on larger-scale dynamical features made techniques based on repeated transects unsuitable. A possible alternative is to use velocity time-series at fixed locations. Three ADCP moorings were operative in the western part of the GoL at the time of the Latex10 campaign. However, their positions were too close to the coast north of Cape Creus, so that they are of limited use for correcting the ship-based velocities collected across the continental shelf margin. For these reasons, in this study, the velocity components associated with NIO have been quantified from Lagrangian drifter trajectories. Here, we use one of the Lyap02 drifters as an example to illustrate the concepts at the basis of the analysis. The same procedure has been applied to the rest of the Lyap01 and Lyap02 drifters. Since the goal is to estimate the NIO components in the GoL, only the portion of each drifter trajectory north of $42°10'$ is included in the analysis.

The trajectory of the central drifter of the Lyap02 array is shown in Figure 5, left (grey line). It is characterized by several clockwise loops, which, as already remarked, indicate the presence of strong NIO. Drifter-based velocities $\mathbf{u}_{drift}$ were computed by finite differencing

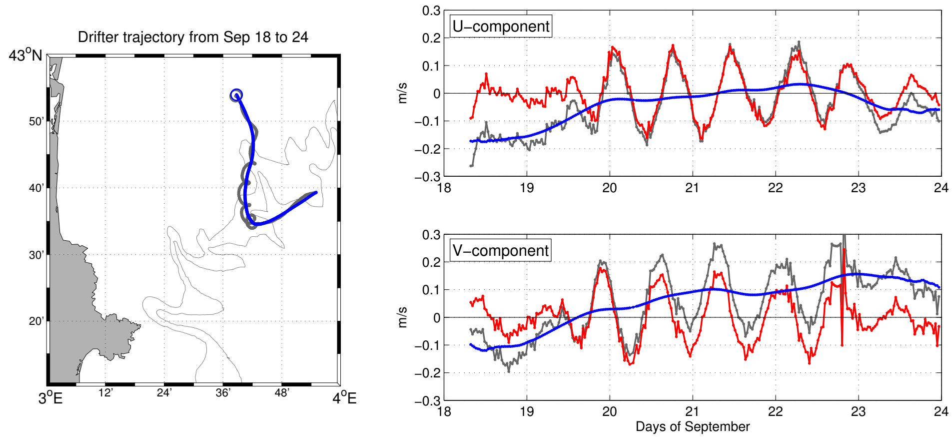

Figure 5. (left) Trajectory of one of the Lyap02 drifters from 18 to 24 September. In grey is the original trajectory, while in blue is the trajectory smoothed with a 17.5 hour moving averaging. The larger circle marks the final position of the drifter on 24 September. (right) Time series of the u- (top) and v-component of velocity (bottom) obtained by finite differencing the drifter trajectory. In grey are the total velocities $\mathbf{u}_{drift}$ and in blue the 17.5 hour moving averaged components $\langle \mathbf{u}_{drift} \rangle$. The NIO components $\mathbf{u}_{NIO}$ (in red) are obtained as difference between the two.

successive drifter positions [e.g. *Poulain et al.*, 2012]. Zonal and meridional components are shown in Figure 5, top and bottom right, respectively (grey lines). Between 20 to 23 September, both time-series evidence large oscillations superimposed to a slowly varying mean. As expected, the oscillations of the two components are out of phase of 90°, with positive meridional components preceding positive zonal ones. Their period is ∼17.5 hours (resulting in almost 3 complete oscillations every 2 days), consistent with the local inertial period.

Following *Haza et al.* [2008], the mean velocity components $\langle \mathbf{u}_{drift} \rangle$ were retrieved by applying a moving average based on a Gaussian window with a full width at half maximum (FWHM) of 17.5 hours. The signal associated with NIO represented the dominant contribution of the residuals components, which were computed as the difference between original and averaged values, $\mathbf{u}_{NIO} = \mathbf{u}_{drift} - \langle \mathbf{u}_{drift} \rangle$. The analysis was also repeated with a 36-hour window (corresponding to two inertial cycles) providing identical results. Mean and residual components are showed in Figure 5, right (blue and red lines, respectively). As also evidenced by the reconstructed mean trajectory (blue curve in Figure 5, left), $\langle \mathbf{u}_{drift} \rangle$ indicates an initial along-slope, southwestern transport, which turned and remained northward (i.e. positive meridional component) after the end of 19 September. During the same period, the $\mathbf{u}_{NIO}$ components are characterized by amplitudes between 0.1 to 0.2 m s^{-1}, the same order of mag-

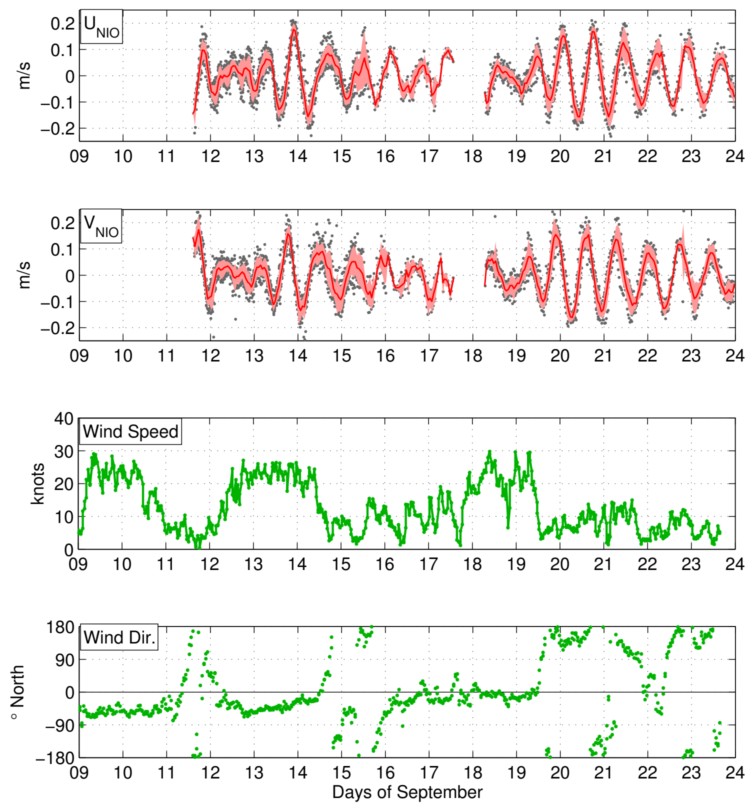

Figure 6. (top) Time series of average NIO velocities $\langle \mathbf{u}_{NIO} \rangle$ (in red) from 9 to 24 September. The velocities were computed by hourly averaging the NIO velocities $\mathbf{u}_{NIO}$ (grey dots) derived from all the available drifters. The red-filled contour marks the one standard deviation confidence interval $\langle \mathbf{u}_{NIO} \rangle \pm \sigma_{NIO}$. The two gaps from 9 to 11 September and from 17 to 18 September correspond to periods when no drifters were operative in the western GoL. (bottom) Time series of the 30 min-averaged wind speed and direction recorded from the *R/V Le Suroît* for the same period.

nitude as the mean meridional velocities, and much larger in the case of the zonal component. Because of that, despite the northward mean transport, instantaneous velocities were characterized by negative meridional velocities in several occasions after 20 September.

The $\mathbf{u}_{NIO}$ components from all the drifters used in the analysis are shown in the top two panels of Figure 6 (grey dots). The time series includes two clusters of observations corresponding to the Lyap01 and Lyap02 deployments. The Lyap01 array included nine drifters deployed on 11 September in the western part of the GoL (Figure 4, top row). After 15 September, five of the drifters were recovered. Within the next days, all the others escaped the GoL south of $42°10'$. Hence, the time series includes observations from a progressively reduced number of drifters with no drifters operative from the afternoon of 17 to 18 September. In the morning of 18 September, the five drifters of the Lyap02 array were deployed across the continental slope (Figure 4, bottom row). These remained in the western GoL until the end of the Latex10 campaign on 24 September.

The time series of the mean $\mathbf{u}_{NIO}$ components $\langle \mathbf{u}_{NIO} \rangle$ were computed by hourly averaging the drifter observations (red lines in Figure 6). These indicate the presence of strong NIO (amplitude > 0.1 m s^{-1}) in the western part of the GoL in two occasions: between 13 and 16 September; and from midday of 19 September to 23 September. Comparison with the 30-minute averaged wind observations from the *R/V Le Suroît* evidences that in both occasions the velocity oscillations occurred after events of strong Mistral/Tramontane winds (Figure 6, bottom two panels). Following *Hu et al.* [2011b], these are identified by wind speed > 15 knots and directions between $-90°$ and $0°$ N. Three of such events occurred between 9 and 11, between 12 and 15 and between 18 and 20 September. The magnitude of the Ekman currents resulting from these strong wind events is of the same order of the reconstructed $\mathbf{u}_{NIO}$ (see supporting information Figure 4). This further support our interpretation of the observed velocity oscillations in terms of NIO. As described in Section 3.1, the first wind event forced the Ekman flow responsible for the initial southward displacement of C waters (Figure 1, bottom left).

The reconstructed NIO time series were used to correct the instantaneous ADCP observations and retrieve the values of the background velocities. First, $\langle \mathbf{u}_{NIO} \rangle$ were linearly interpolated in time to match ADCP observations. Then, at any given time, background velocities were simply computed as the difference between ADCP and the corresponding NIO component, $\tilde{\mathbf{u}}_{tr} = \mathbf{u}_{tr} - \langle \mathbf{u}_{NIO} \rangle$ (note that this way, signatures from high-frequency processes were also removed from the background velocity). As $\langle \mathbf{u}_{NIO} \rangle$ is derived from drifter trajectories very close to the various transects, this correction is expected to be relatively accurate. Nonetheless, it might introduce uncertainties related to the spatial variations of NIO (for instance through their interaction with small-scale dynamics [e.g. *Weller*, 1982; *Klein and Hua*, 1988]). To account for the impact of such uncertainties on the precision of our volume transport estimates, σ_{NIO} (the standard deviation of $\langle \mathbf{u}_{NIO} \rangle$) has been included in the error analysis presented in Appendix A.

As an example, Figure 7 shows the impact of such correction on the 15 m depth ADCP velocities collected along transects D2 and D3 from group D (see position of the transect in Figure 4, bottom row). Transect D2 was collected from west to east, and transect D3 in the

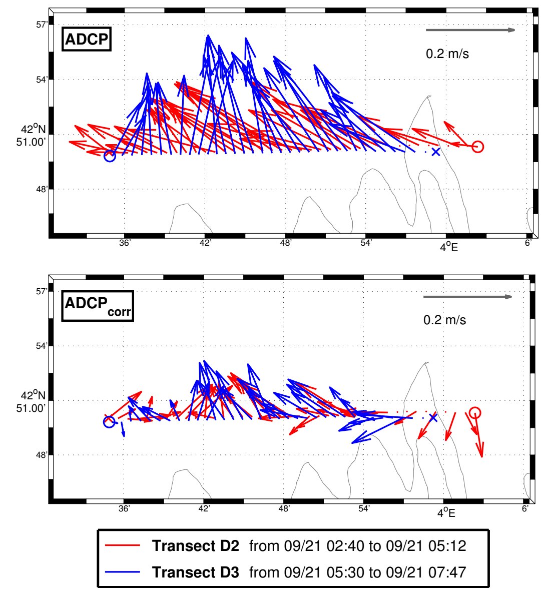

573 **Figure 7.** (top) Vectors of the instantaneous ADCP velocities $\mathbf{u}_{tr}$ for two successive transects (in red and blue, respectively) from group D (see transect position in Figure 4, bottom row). The beginning and the end of each transect are marked by a cross and a circle, respectively. Transect D2 was collected from west to east, whereas transect D3 from east to west. ADCP vectors are plotted one every four. (bottom) Corrected velocity vectors $\tilde{\mathbf{u}}_{tr}$ for the same transects obtained by subtracting the NIO components from Figure 6 from the instantaneous ADCP measurements.

opposite direction, both in the morning of 21 September. Instantaneous ADCP velocities are shown in the top panel. From the beginning of transect D2 to the end of transect D3, the vectors are clearly characterized by a clockwise rotation with time. Their zonal component progressively decreases until eventually shifting sign. At the same time, their meridional component reaches its maximum magnitude ($\sim$ 0.2 m s^{-1}), before gradually decreasing again. Both variations are consistent with the phase of the NIO components in Figure 6. On the other hand, the corrected velocity vectors (bottom panel) show a better coherence between the two transects. Furthermore, the largest meridional components are sensibly reduced to $\sim$ 0.1 m s^{-1}, consistent with the averaged velocities retrieved for the same period from the Lyap02 drifter trajectories (Figure 5, right).

Due to the gaps in the mean residual time series, only instantaneous ADCP velocities from groups B and D could be corrected. Groups A and C were collected at the beginning of 11 September and between 17 and 18 September, respectively, when no drifters observations were available in the western GoL. The implications for the quantification of the along-front cross-shelf fluxes associated with those groups are discussed in more detail in the next Section.

3.4 Cross-shelf Exchanges

3.4.1 Identification of the exchanged waters along the transects

Figures 8 to 11 show the portion of the first transect of groups A to D within which the different water masses described in Section 3.2 have been detected. These have been identified from the observations of surface temperature and salinity (top and middle panels) using the thresholds defined in Section 3.2. The 15-m depth meridional components of the ADCP velocities (corrected for NIO in case of groups B and D; bottom panels) were also included as an identification criteria to further distinguish outflowing GoL shelf waters (U and C) and inflowing open NW Mediterranean waters (C).

The outflow of GoL shelf waters within group A transects included U waters only. These are identified by SST$<$ 19.5°C, SSS$<$ 38.1 psu and negative meridional velocities (Figure 8). Such outflow occupied a large portion of each transect (from $\sim$3.7 to beyond 4°E for the first one; from $\sim$3.75 for the second one). West of 3.7°E, the transect indicates an outflow of waters with characteristics similar to C waters (SST$<$ 20.1°C, SSS$<$ 38.1 psu). However, without nearby drifter trajectories and clear signature from pseudo-SST imagery, their origin can-

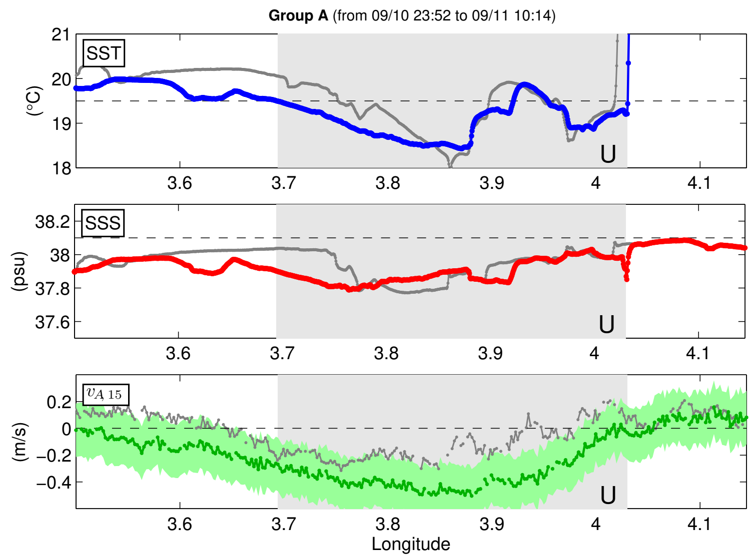

Figure 8. (top) Surface temperature, (middle) surface salinity and (bottom) 15-m meridional velocity component for group A (Figure 4, top row). Two successive transects were collected. As in Figure 4, the first one is in color, the other in grey. The gray area marks the portion of the first transect along which the upwelled (U) waters escaped the GoL. It is identified by SST and SSS values below the limits of Figure 4, 19.5° and 38.1 psu respectively (dashed lines), and by negative meridional velocities. The eastern boundary of the gray area marks the front between U waters and the warmer central NW Mediterranean waters. Waters between 3.9 and 3.95°E, characterized by higher SST than U, were not included in the computation of the total exchanges (see Figure 12). ADCP velocities were not corrected for NIO. The confidence interval $v_{A,15} \pm \delta v_A$ (defined in Appendix A) for the first transect of the group is marked in light-green.

not be accurately determined. To avoid overestimating the outflow from the continental shelf, we preferred not to include them in the computation of cross-shelf exchanges. For the same reasons, the filament of warmer waters observed between 3.9 and 3.95°E was also excluded (see also Figure 12). As explained in Section 3.3, ADCP meridional velocities from group A could not be corrected for NIO, due to the lack of Lagrangian observations before the afternoon of 11 September. The instantaneous meridional velocities are characterized by the highest values (~ 0.5 m s^{-1}) among all groups, as well as by the largest variations between successive transects, despite the two being collected back and forth along the same track (Figure 8, bottom). Since the wind time series from Figure 6 suggests the possibility of strong NIO at the time of group A observations, it is likely that such variations were the direct result of the change of phase of NIO while the two transects were collected. Indeed, the successive passages over transects A1 and A2 spanned roughly 10 and a half hours, $\sim 60\%$ of the local inertial period. As such, velocity errors for these transects are assumed of the same order as the NIO-components, rather than σ_{NIO} (see Appendix A).

Group B transects were characterized by an outflow of combined U and C waters, identified by SST< 20.1°C, SSS< 38.1 psu and negative meridional velocities (Figure 9). The portion of the transects occupied by the outflow had a similar width as in group A, but its position was shifted to the West. C waters extended from around 3.5 to 3.7°E, where U waters appeared. These extended to 3.8°E in the first transect, and around 3.9°E in the other two. Despite the large NIO observed at the time of group B, the corrected meridional velocities show more consistency between successive transects than the instantaneous velocities from group A (Figure 9, bottom). This further supports the importance of NIO corrections for retrieving reliable estimates of the background flow leading to more accurate quantifications of the cross-shelf fluxes.

As opposed to the previous two groups, the outflow of GoL shelf waters from group C transects was not characterized by U waters, but by C waters only. Like in group B, it is identified by SST< 20.1°C, SSS< 38.1 psu and negative meridional velocities (note that south-flowing waters from Group C are always characterized by SST> 19.5°C and SSS> 37.85 psu, the two lower thresholds for C waters; Figure 10). The outflow of C waters occupied a similar portion as in group B, extending from $3.5°$ to 3.7°E in the first transect, and to around 3.8°E in the others. As for group A, the meridional velocities could not be corrected for NIO (Figure 10, bottom). Nonetheless, velocities from successive transects show a consistency analogous to those observed for the corrected velocities from group B. This is not entirely surpris-

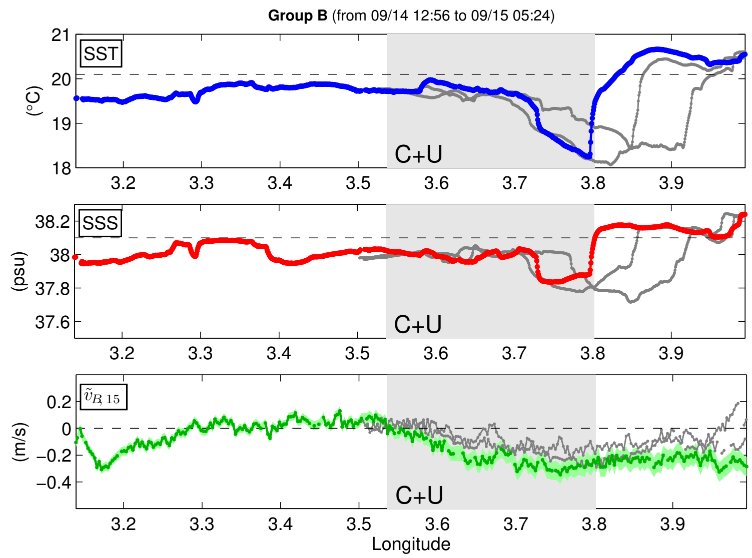

646 **Figure 9.** Same as Figure 8, but for group B (Figure 4, second row). A total of 3 transects were collected.
647 The gray shaded area indicates the portion of outflowing upwelled (U) and continental shelf (C) waters within
648 the first transect. It is identified by SST and below 20.1° and 38.1 psu respectively (dashed lines), and by
649 negative meridional velocities. The eastern boundary of the gray area marks the front between C+U and O
650 waters. ADCP velocities were corrected for NIO. The confidence interval $\tilde{v}_{B,15} \pm \delta v_B$ (defined in Appendix
651 A) for the first transect of the group is marked in light-green.

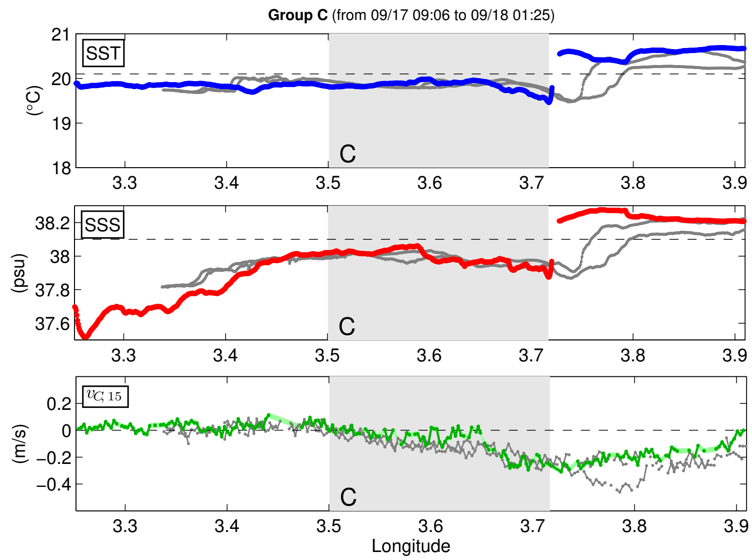

Figure 10. Same as Figure 8, but for group C (Figure 4, third row). A total of 3 transects were collected. The gray shaded area indicates the portion of outflowing continental shelf (C) waters within the first transect. It is identified by SST and below 20.1° and 38.1 psu respectively (dashed lines), and by negative meridional velocities. The eastern boundary of the gray area marks the front between C and O waters. ADCP velocities were not corrected for NIO. The confidence interval $v_{C,15} \pm \delta v_C$ (defined in Appendix A) for the first transect of the group is marked in light-green. The data gap along the first transect is due to ship operations (i.e. CTD profiling) during which the thermosalinograph was turned off. ADCP velocities were also discarded, as their accuracy dropped significantly while the vessel maintained a fixed position.

ing, since the Lagrangian observations from 17 to 18 September suggest much weaker NIO (~ 0.05 m s^{-1}) at the time of group C than for the previous two groups. For this reason, velocity errors for these transect were assumed to be of the same order as the instrument precision (see Appendix A).

Finally, group D transects are characterized by the northward flow of O' waters (O waters modified by the storm events between 18 and 19 September), identified by SST> 19.6°C, SSS> 38.05 psu and positive meridional velocities (Figure 11). As such, group D is the only group from which it is possible to estimate the inflow of open NW Mediterranean waters into the GoL continental shelf. Compared to the outflows from the other groups, the inflow occupies a more limited longitudinal portion: for all four transects of group D, it extends from 3.7 to slightly beyond 3.8°E. As for group B, the velocities from group D were corrected for NIO. The corrected meridional components show again good consistency between successive tran-

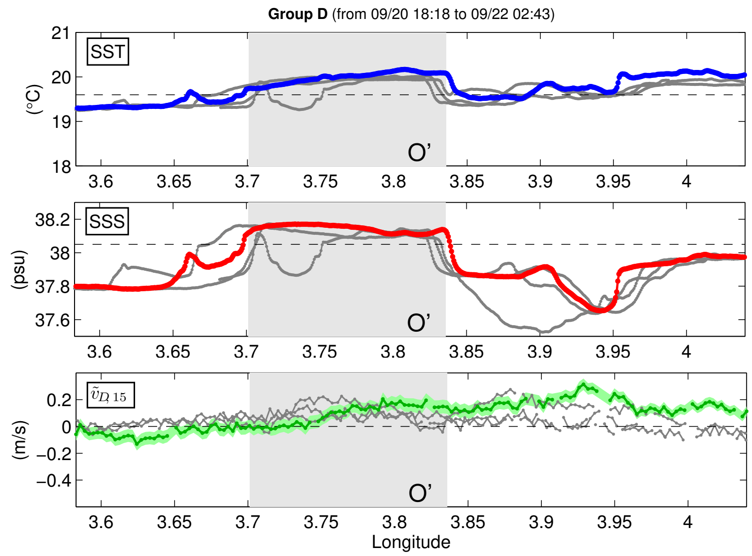

Figure 11. Same as Figure 8, but for group D (Figure 4, last row). A total of 4 transects were collected. The gray shaded area indicates the portion of inflowing open NW Mediterranean (O') waters within the first transect. It is identified by SST and SSS values above 20.1° and 38.1 psu respectively (dashed lines), and by positive meridional velocities. The western boundary of the gray area marks the front between C and O waters. ADCP velocities were corrected for NIO. The confidence interval $\tilde{v}_{D,15} \pm \delta v_D$ (defined in Appendix A) for the first transect of the group is marked in light-green.

sects despite the presence of NIO of the same order of magnitude as the mean background velocities (between 0.1 and 0.2 m s^{-1}) at the time of observations (Figure 11, bottom).

3.4.2 Quantification of group volume transports and total cross-shelf exchanges

The distribution of $(VT_{tr})_i$ (the cross-shelf volume transport associated with a single observation defined in equation 3) for each transect from groups A to D is shown in Figure 12. The resulting total transports VT_{tr} and the associated errors are indicated in the legends. As mentioned in Section 2.3, VT_{tr} was computed by integrating the meridional velocity components (instantaneous $v_{tr,15}$ for groups A and C; corrected $\tilde{v}_{tr,15}$ for groups B and D) along each cross-front transect. Transect collected along non-zonal directions were projected accordingly.

Among the four groups, the fluxes computed for group A (Figure 12, top panel) are characterized by the largest variability. Maximum values of $(VT_{tr})_i$ vary from $\sim -2\ 10^{-3}$ Sv in transect A1 to between $\sim -1.25\ 10^{-3}$ Sv in transect A2, few hours later. The resulting VT_{tr} of U waters drops from -0.194 ± 0.129 to -0.058 ± 0.073 Sv. Since it was not pos-

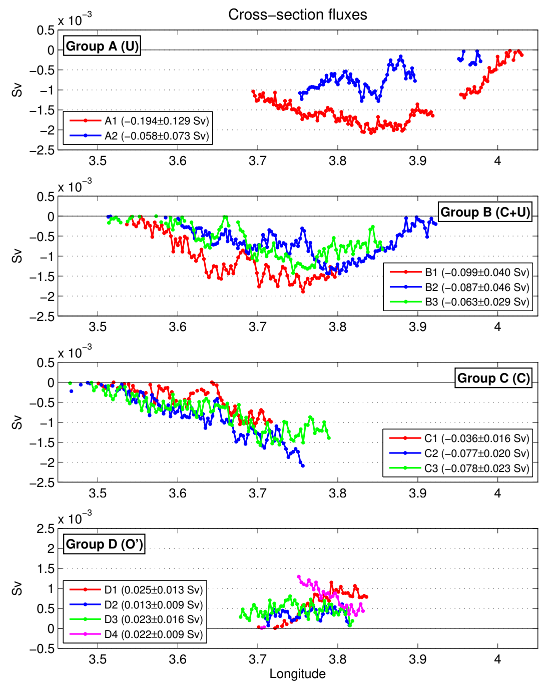

Figure 12. Distribution of the cross-section fluxes $(VT_{tr})_i$ (Equation 3) from each individual ADCP measurements along the transects of the four groups from Figure 4. The measurements were corrected for NIO for Groups B and D. For each transect, the total fluxes VT_{tr} (Equation 2) and the associated errors δVT_{tr} (Equation A.5) are shown in the legend of each panel. The negative fluxes in the top three panels are associated with outflow of upwelled (U) and/or continental shelf (C) waters from the GoL. The positive fluxes in the bottom panel are associated with inflow of open NW Mediterranean (O') waters. The gap in group A corresponds to a filament of waters characterized by higher SST than U (see Figure 8). Their contribution (a total of 0.023 Sv for transect 1 and 0.008 Sv for transect 2) was therefore excluded from the computation of the total exchanges. Southward waters flowing West of 3.7 with TS characteristics different that U waters were also excluded (total transport of 0.050 Sv for transect 1 and 0.030 Sv for transect 2). For reference, 0.1° in longitude corresponds to a Δl of ~8.2 km at the GoL latitudes.

sible to correct group A velocities for near-inertial currents, such difference in VT_{tr} within a short time interval, as well as the associated large errors, are a direct consequence of the NIO-induced variations in the instantaneous ADCP meridional velocities already evidenced in Figure 8. This further confirms the importance of correcting the instantaneous velocities for NIO components in order to obtain reliable estimates of cross-shelf fluxes from ship-based observations. Averaging VT values from successive passages over the same section can partially reduce the impact of NIO and provide a more accurate quantification of the fluxes associated with the mean currents. The average VT for group A is -0.126 ± 0.074 Sv. The error was computed from equation A.6. Although the relative error is reduced compared to the individual transects, with only two repeated transects the precision of the VT estimate for group A remains much lower than for the other groups (see also Figure 13).

Cross-shelf fluxes based on the corrected velocities from group B (second panel from top) show less variability between successive transects. The fluxes are characterized by similar values and along-transect profiles. The relative errors are smaller compared to group A, ranging between 40.6 and 53.1%. The main difference from one transect to the other is in the position of the profiles: for instance, the maximum values of cross-shelf outflow shift from slightly after 3.7 °E in transect B1 to 3.8 °E in transect B2. Part of this variation can be explained by the fact that the transects were not located along the same latitudinal tracks. In particular, transect B2 intersected the front axis further north than the other two (see Figure 2). The resulting eastward shift of the region of maximum outflow is consistent with the NNE-SSW orientation of the front axis retrieved from the Lyap01 deployment. Furthermore, transect B2 was collected closer to the estimated position of the hyperbolic point [see also *Nencioli et al.*, 2011]. This can at least partially explain the slight decrease in the values of maximum velocities from transect B1 to B2 (see also Figure 9, bottom). At the same time, such weakening is associated with a widening of the region occupied by U and C waters, consistent with a broader but less intense outflow closer to the hyperbolic point. As discussed in Section 2.3, along-front velocities tend to increase away from the hyperbolic point inducing a stretching of the water mass along the attracting LCS and a narrowing of its width across the LCS axis, so that the total VT remain similar for different sections along the LCS [see also *Nencioli et al.*, 2013]. The resulting outflows of combined U and C waters for the three transects are -0.099 ± 0.040, -0.087 ± 0.046 and -0.063 ± 0.029 Sv, respectively. It is important to remark that the same analysis performed with uncorrected instantaneous velocities results in

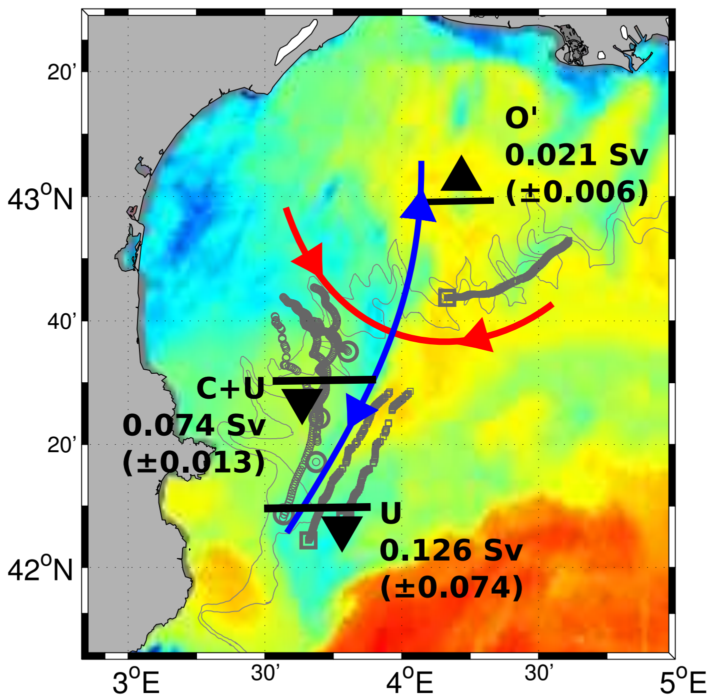

Figure 13. Schematics of the average cross-shelf fluxes associated with the front, superimposed on pseudo-SST (shaded), buoy trajectories (grey) and LCSs (red and blue) from Figure 1. The errors within brackets are computed from Equation A.6. Locations of outflow and inflow of the various waters are all indicated relative to the Lyap01 LCS, as no cloud-free pseudo-SST images are available for the period of Latex10 after 15 September. These values are the average from the two transects of group A for the outflow of U waters; from the six transects of groups B and C for the outflow of U+C waters; and from the four transects of group D for the inflow of O' waters. Integrated over the observed front lifetime of two weeks, these resulted in total mixed layer water exchanges of 90 ± 14 and 25 ± 7 km^3 out from and into the GoL, respectively.

relative differences in VT_{tr} estimates of the same order as the one observed for group A (not shown).

Despite being computed from instantaneous meridional velocities, cross-shelf fluxes from group C (Figure 12, third panel from top) show similar values and profiles for all three transects. Moreover, the resulting VT_{tr} for the outflow of C waters (-0.036 ± 0.016, -0.077 ± 0.020 and -0.078 ± 0.023 Sv, respectively) are consistent with the ones from group B. This further indicates that, due to weaker NIO between 17 and 18 September (characterized by smaller magnitude than the background mean flow), fluxes could be reliably computed for group C even without velocity corrections. The difference between the VT from transect C1 and transects C2 and C3 is only marginally induced by variations in the velocity profile. Instead, it mainly results from a broadening of the region occupied by C waters towards the front axis, where meridional velocities are stronger (see also Figure 10; the shaded area corresponds to C1).

The inflow of O' waters in group D is much smaller than the outflows in the previous groups. This is due to both weaker meridional velocities, as well as to the narrower region occupied by the intruding O' waters. Because of that, relative errors are slightly higher, ranging between 40.5 and 70.3%, since the velocity uncertainties remain of the same order as group B. The much narrower width of transect D4 is due to a further reduction of the presence of O' waters, replaced to the west by water masses with different T-S characteristics (see also Figure 11). Total VT_{tr} for the four transects are 0.025 ± 0.013, 0.013 ± 0.009, 0.023 ± 0.016 and 0.024 ± 0.009 Sv. These estimates were obtained with corrected velocities. As for group B, the same analysis performed with instantaneous velocities returns a much broader range of VT_{tr} values (not shown).

A schematics with the average values of VT for the different water masses is shown in Figure 13. Outflow of U waters (-0.126 ± 0.074 Sv) was computed from the two transects of group A; outflow of combined C and U waters (-0.074 ± 0.013 Sv) from the six transects of groups B and C; inflow of O' waters (0.021 ± 0.006 Sv) from the four transects of group D. As described for group 1, the combined errors are computed by dividing the sum in quadrature of the individual errors of each transects by the total number of transects considered. The combined relative errors are 59, 17 and 29% respectively. As illustrated in the figure, the quantified flows from and to the GoL were associated with specific sides of the *in-situ* LCS from *Nencioli et al.* [2011]: outflow from group A extended across the southern attracting LCS; outflow from groups B and C occurred west of the southern attracting LCS; inflow from group D occurred east of the northern attracting LCS.

The cross-shelf exchanges associated with the Latex10 front can be computed by integrating the estimated VT over its lifetime. As reported in *Nencioli et al.* [2011], the position of the *in-situ* LCS (and hence of the front) was tracked and reconstructed from 12 to 24 September. Unfortunately, due to a lack of Lagrangian observations and cloud-free satellite imagery, it is not possible to know for how much longer the front persisted in the western part of the GoL after 24 September. A conservative estimate of the total along-front exchanges can be obtained by assuming a front lifetime of two weeks. The resulting outflow of combined C and U waters (from the average VT from groups B and C) amounts to $\sim 90{\pm}14$ km^3, whereas the inflow of O' waters (from the average VT of group D) to $\sim 25 \pm 7$ km^3.

4 Discussion and Conclusions

In this study, we have quantified the cross-shelf exchanges associated with a front observed in the western part of the GoL during the Latex10 campaign (September 2010). Our approach combined ship-based measurements, Lagrangian drifter trajectories and remote sensing observations. The analysis of pseudo-SST imagery and drifter trajectories revealed that the formation of the front was associated with the convergence of three distinct water masses: U, C and O (O' after 19 September). These were advected along repelling and attracting LCS, identified *in-situ* across the continental slope by the trajectories of two drifter arrays. The surface temperature and salinity characteristics of the water masses were identified from ship-based thermosalinograph observations. These values provided thresholds to determine the presence of each water mass along a series of cross-front transects clustered into four distinct groups. As the front was associated with the attracting LCS, ADCP velocities collected along those groups were used to compute the cross-shelf exchanges resulting from the along-front advection of the different water masses. Due to the presence of strong NIO, the instantaneous ADCP observations could not be directly applied in the computation. First, NIO currents were estimated from the drifter trajectories and their contribution subtracted from the instantaneous ADCP velocities. The resulting corrected currents were then integrated to obtain more accurate estimates of the fluxes induced by the background mean flow.

Our results showed average outflow from and inflow to the GoL of $\sim 0.074 \pm 0.013$ Sv and $\sim 0.021{\pm}0.006$ Sv, respectively. The outflow was associated with the southward advection of U and C waters; the inflow with the northward advection of O' waters. Integrated over a conservative estimate of the front lifetime of two weeks, these along-front fluxes resulted in $\sim$ 90 $\pm$ 14 km^3 of exported U and C waters, and $\sim$ 24 $\pm$ 7 km^3 of imported O' waters. By defining the 200 m isobath as its outer boundary, the GoL is characterized by an area of roughly 13030 km^2. Assuming an average MLD of 22.8 m, the total volume of its upper mixed layer waters is about 300 km^3. According to our results, the fluxes associated with processes such as the front observed during Latex10 are thus capable of inducing the export of 25 to 35% of the GoL upper waters: 3 to 4 of such events are sufficient to completely renew its upper mixed layer.

The observations presented in this manuscript suggest that cross-shelf exchange events such as the one we observed, resulted from a combination of wind-driven and intrinsic geostrophic dynamics, which are quite typical for the western part of the GoL. Therefore, they are probably an important contributor, along with dense shelf water cascading [*Canals et al.*, 2006; *de Madron et al.*, 2013], to the total water budget of the GoL. However, future work is still required to characterize the dynamics of such events and their frequency of occurrence in detail. Nevertheless, because of the large upper water exchanges induced, these processes are likely a key regulator of the biogeochemical and ecological conditions of the GoL. In particular, due to the existing strong cross-shelf biogeochemical gradients, their spatio-temporal distribution could strongly impact nutrient availability and, hence, phytoplankton dynamics over the continental shelf, providing a substantial contribution to the intermittent blooming conditions observed in the region [*D'Ortenzio and Ribera d'Alcalà*, 2009].

The induced inflow of open sea waters was not as strong as the outflow of shelf waters. It represented only 5 to 10% of the total volume of upper layer waters. To maintain the volume balance, larger inflows must occur either at depth or in the eastern part of the GoL. Further studies at the regional scale based on remote sensing observations and numerical models will be required to address this issue, as well as to investigate the role played by other meso- to submesoscale processes [such as the frequently observed eddies; e.g. *Hu et al.*, 2011b; *Kersalé et al.*, 2013] and their spatio-temporal variability in regulating cross-shelf exchanges. In particular, results from a high-resolution regional model focusing on winter-spring 2011 [*Juza et al.*, 2013] showed cross-shelf fluxes in line with the values obtained in this study (if the integration depth in Equation 1 is adjusted to a completely mixed water column typical of winter conditions). This suggests that analogous model configurations might be successfully used for future basin-scale multi-annual analyses of cross-shelf exchanges in the NW Mediterranean.

Like previous works based on the observations from the Latex10 campaign [*Nencioli et al.*, 2011, 2013], our study demonstrates the critical role of an adaptive sampling strategy for the *in-situ* investigation of short-lived, localized processes. Furthermore, it evidences the importance of a multi-platform approach for the interpretation and quantification of the cross-shelf exchanges along the front. Our analysis would have been seriously limited without integrating together remote sensing observations, ship-based measurements and Lagrangian drifter trajectories. For instance, the ship-based thermosalinograph measurements between 10 and 20 September would have been too complex to interpret alone, without the larger context about origin and movements of the different water masses provided by remote sensing and Lagrangian observations. Similarly, the pseudo-SST maps from Figure 3 alone could not provide enough information to reliably quantify the cross-shelf exchanges between 3 and 8 September. For instance, although showing the presence of a tongue of warm water in the eastern part of the GoL on 8 September, pseudo-SST maps do not provide clear indication whether it was entirely due to the intrusion of O waters or also partially resulting from an eastward displacement of the warmer waters from the western part of the shelf. Analogously, despite showing colder waters appearing in the western part of the GoL on 8 September, they do not provide any further indication to distinguish the contribution in their formation due to surface water cooling after the Mistral/Tramontane event from that due to the southern outflow of surface waters out of the GoL.

Combining ship-based and Lagrangian *in-situ* observations played a key role within our multi-platform approach. Dispersion patterns of the Lagrangian drifters provided complementary indications on the front position (through *in-situ* LCS) and on the movements of the different water masses, particularly important when satellite imagery failed due to cloud coverage. Furthermore, the identification of the *in-situ* LCS allowed the use of cross-front transects that were neither at the GoL boundary nor parallel to its direction to quantify the cross-shelf exchanges associated with the advected water masses. Finally, drifter trajectories provided the possibility to estimate the intensity of NIO currents independently from ship-based ADCP velocity measurements. This is a critical aspect for any study aiming at quantifying cross-shelf exchanges associated with localized and rapidly evolving processes, since it greatly reduces the need of repeated transects along a given section and hence the time needed to obtain accurate estimates of the fluxes induced by the background mean flow.

The main source of uncertainties of our analysis are associated with the reconstructed NIO velocities, the estimates of the MLD and those of the front direction. Uncertainties associated with the front direction determine small errors in the computed volume transport, usually of the same order or smaller than those due to MLD uncertainties (the only exception is transect C1). This is likely due to the fact that the corrected velocities are characterized by small zonal components and that the cross-front transects were collected mainly along the zonal direction.

The cross-shelf exchanges associated with the Latex10 front have been quantified using only observations at a fixed depth. Ship-towed profilers, as well as ADCP measurements with higher vertical resolution and better coverage of the first few meters of the water column should be included in future campaigns focusing on the investigation of cross-shelf exchanges. These can provide more detailed observations of the vertical distribution and the dynamics of the different water masses throughout the water column. Such observations could help to better assess the contribution of the vertical dynamics associated with secondary ageostrophic circulation in driving the exchanges, leading to more robust dynamical constraints for the assumptions at the base of the analysis. They would also reduce some of the uncertainties in the quantities used to compute the volume transport, resulting in more refined estimates.

At the same time, the contribution of NIO uncertainties on the total error is of the same order (usually slightly higher) as that of the MLD (see supporting information Figure 8). Thus, improved accuracy of the corrected mean velocities would also be needed to obtain further significant improvements in the accuracy of the cross-shelf estimates. Although this represents a challenging task, the deployment of a larger number of drifters combined with one or more ADCP moorings within the region of study could provide more accurate estimates of the near-inertial (as well as tidal) currents and their spatial variability. Future campaigns will also benefit from upcoming satellite missions based on new generation altimeters [e.g., Surface Water and Ocean Topography, SWOT; *Fu and Ferrari*, 2008], which will provide cloud-free velocity fields at higher resolution than current altimeters, and more reliable within coastal regions. Integrated with the imagery of surface tracers such as SST and ocean color, these will provide a critical contribution for the further development of the analysis of the mixed-layer cross-shelf exchanges induced by mesoscale (and possibly submesoscale) processes at both the global and the regional scale.

A: Error analysis on volume transport estimates

The main sources of error in the computation of the along-front fluxes from the discretized version of equation 1 include the uncertainties associated with a) the definition of the integration limits along each transect, δl_{ini} and δl_{end}; b) the estimates of the MLD, δz; c) the corrected meridional velocities, $\delta \tilde{v}_{tr,15}$; d) the direction of integration, $\delta \hat{\mathbf{n}}$

The integration limits l_{ini} and l_{end} have been defined in Section 3.4 based on the TS characteristics of the different water masses and the orientation of the corrected meridional velocities. Since the transitions between the different water masses are characterized by sharp gradients, uncertainties associated with the identified SST ans SSS thresholds will results in δl_{ini} and δl_{end} of only few bins. When the water mass boundaries along a transect are defined by the orientation of the corrected meridional velocities (as for the western boundary of C waters in group B), uncertainties in $\tilde{v}_{tr,15}$ can determine larger δl_{ini} and δl_{end}. However the additional bins included in (or removed from) the flux computation will be characterized by small values of $\tilde{v}_{tr,15}$ (maximum values cannot exceed the velocity uncertainties defined in the next paragraph). Hence, in both cases, the uncertainties associated with the integration limits will determine only minimal variations of the computed volume transport.

The other three source of uncertainty are all expected to have a significant contribution to the errors associated with the volume transport estimates, and thus they are all included in the error propagation analysis. The uncertainty associated with the MLD has been quantified in section 2.3 as the standard deviation of the mixed-layer depth from the 21 CTD profiles collected during Latex10, so that $\delta z = 4.8$ m. Uncertainties in the corrected meridional velocities are due to three factors: the instrument precision, the horizontal and vertical variability within each transect bin and the inaccuracy in the drifter-derived NIO components. Following *Petrenko et al.* [2005], the uncertainty due to the precision of the processed ADCP velocities is better than 0.02 m s^{-1}. Given the resolution of each transect (the length of each bin is $\sim$ 250 m) and the low vorticity Rossby numbers associated with each transect (see supporting information Figure 6), the uncertainties due to the horizontal velocity variations within each bin can be reasonably assumed to be much lower. The same holds for the vertical variations. Indeed, as already mentioned in section 2.3, comparison between the velocities at 15, 19 and 23 m supports our hypothesis of nearly vertically-uniform velocities within the upper mixed layer (see supporting information Figure 2). On the other hand, the uncertainties due to the NIO-component correction are much larger and correspond to $(\sigma_{NIO})_i$, the standard deviation of $\langle v_{NIO} \rangle$ at each ADCP observation (figure 6). Values along the various transects range from ~0.03 to more than 0.07 m s^{-1}.

The uncertainties in the drifter-derived NIO components dominate the velocity error for group B and D transects, for which the velocity correction was applied. Thus, $\delta v = (\sigma_{NIO})_i$. On the other hand, group A and C transects require specific considerations. Due to the lack of drifter observations, estimates from both groups were obtained using instantaneous ADCP velocities. The mistral event on the September 9-10 and the reconstructed NIO time series before September 12 suggest the presence of relatively strong NIO at the time Group A transects were collected. The velocity error for those transects can be thus assumed to be of the same order as the NIO-components, so that $\delta v_{tr} = 0.20$ m s^{-1}. On the other hand, group C transects were collected during weak NIO. Because of that, the velocity error is assumed to correspond to the instrument precision, so that $\delta v_{tr} = 0.02$ m s^{-1}.

Finally, in deriving equations 2 and 3, we assumed $\hat{\mathbf{n}}$ to be oriented North to South, although the direction of the LCS identified from the Lyap01 array was NNE-SSW. Thus, the uncertainty in the $\hat{\mathbf{n}}$ direction can be assumed to be 15°, so that the error analysis will also assess the sensitivity of the computed fluxes to our direction assumption.

The analysis of the propagation of these three sources of uncertainty in our volume transport estimates requires two steps: first, the errors associated with the volume transport at each bin are computed; second, these are combined together to quantify the error associated with the total transport of each transect.

To quantify the contributions of the different uncertainties, we must consider the general equation for the cross-shelf volume transport associated with each observation, defined as

$$(VT_{tr})_i = |\tilde{\mathbf{V}}_{tr,15}|_i \cos\theta \; |\Delta\mathbf{L}|_i \sin\alpha \; \Delta z \tag{A.1}$$

where $|\tilde{\mathbf{V}}_{tr,15}|_i$ is the magnitude of the total corrected velocity; θ the angle between the corrected velocity and $\tilde{\mathbf{n}}$; $|\Delta\mathbf{L}|_i$ the total distance between successive bins; and α the angle between the ship track and $\tilde{\mathbf{n}}$. Note that by choosing $\tilde{\mathbf{n}}$ to be oriented to the North, $|\tilde{\mathbf{V}}_{tr,15}|_i \cos\theta$ becomes $(\tilde{v}_{tr,15})_i$ and $|\Delta\mathbf{L}|_i \sin\alpha$ becomes $(\Delta l)_i$, so that equation A.1 reduces to equation 3.

Since MLD, velocity and front direction estimates are independent (i.e. misestimates of one do not affect the estimates of the others), the relative contribution of their uncertainties can be summed in quadrature, so that the error associated with each $(VT_{tr})_i$ is

$$(\delta VT_{tr})_i = |(VT_{tr})_i| \sqrt{\left(\frac{\delta v_{tr}}{\tilde{v}_{tr,15}}\right)_i^2 + \left(\frac{\delta z}{\Delta z}\right)^2 + \left(\frac{\partial (VT_{tr})_i}{\partial \theta}\Delta\theta\right)^2 (VT_{tr})_i^{-2}} \tag{A.2}$$

Since θ and α covary with $\tilde{\mathbf{n}}$, the last term accounts for the uncertainties of both. Due to the non-linearity of cos (and sin) around 0 and π ($\pi/2$ and $3\pi/4$), the derivative in the last term was quantified as

$$\frac{\partial (VT_{tr})_i}{\partial \theta}\Delta\theta = (\cos(\theta+\Delta\theta)\ \sin(\alpha+\Delta\theta) - \cos\theta\sin\alpha)\ |\tilde{\mathbf{V}}_{tr,15}|_i\ |\mathbf{\Delta L}|_i\ \Delta z \tag{A.3}$$

Examples of the distribution of $(\delta VT_{tr})_i$ and the individual contribution of the three sources of uncertainties along various transects are provided in the supporting information.

If the various errors $(\delta VT_{tr})_i$ are assumed to be independent from each other, the total error associated with the transect volume transport VT_{tr} (equation 2) is given by their sum in quadrature

$$\delta VT_{tr}\Big|_{min} = \sqrt{\sum_{i=1}^{n}(\delta VT_{tr})_i^2} \tag{A.4}$$

Due to the large number of observations n along each transects the resulting total errors are relatively small, ranging from 2.8 to 12.3 % for different VT_{tr}. At the same time, it is unlikely for the errors $(\delta VT_{tr})_i$ to be completely independent: for instance, over(under)estimates of the MLD, resulting in over(under)estimates of $(VT_{tr})_i$, are likely to persists for several bins in a row along a transect. Thus, a more conservative estimate of the total error can be obtained by the simple sum of each error from equation A.2:

$$\delta VT_{tr}\Big|_{max} = \sum_{i=1}^{n}(\delta VT_{tr})_i \tag{A.5}$$

The resulting total errors are much larger than the ones from equation A.4, ranging from 25.6 up to 111.3% for different VT_{tr}.

The total errors presented throughout the paper come from equation A.5. They are an overestimate of the true total error, since they represent its highest threshold in case of perfectly correlated $(VT_{tr})_i$. Since $(VT_{tr})_i$ are neither completely independent nor completely correlated, the true value of the total error for each transect lies between $\delta VT_{tr}|_{max}$ and $\delta VT_{tr}|_{min}$ (representing its minimum threshold). A summary of the error analysis, with total error values for each transects, is provided in table A.1.

The VT_{tr} estimates for the various transect can be assumed to be independent. Indeed, our CTD observations suggest that the deviations from the average MLD were not systematic

Table A.1. Minimum and maximum thresholds (in Sv) for the total error associated with the volume transport of each transect. The number of observations (n) used for each transect are indicated in the third column. Values between brackets indicate the relative error as a percentage of the corresponding volume transport. Values of $\delta VT_{tr}|_{max}$ are the ones presented throughout the paper.

Group	Transect	n	$\lvert VT_{tr}\rvert$	$\delta VT_{tr}\|_{min}$	$(\%VT_{tr})$	$\delta VT_{tr}\|_{max}$	$(\%VT_{tr})$
A	1	141	0.194	0.011	(5.6)	0.129	(66.5)
	2	82	0.058	0.008	(14.0)	0.073	(126.0)
B	1	91	0.099	0.004	(4.3)	0.040	(40.6)
	2	129	0.087	0.004	(4.8)	0.046	(53.1)
	3	99	0.063	0.003	(4.6)	0.029	(45.9)
C	1	75	0.036	0.003	(7.0)	0.016	(46.2)
	2	88	0.077	0.002	(3.0)	0.020	(26.1)
	3	99	0.078	0.002	(3.1)	0.023	(29.0)
D	1	39	0.025	0.002	(8.2)	0.013	(51.3)
	2	37	0.013	0.002	(11.6)	0.009	(70.3)
	3	50	0.023	0.002	(9.6)	0.016	(67.6)
	4	30	0.022	0.002	(7.5)	0.009	(40.5)

across a given transect nor specific to certain dynamical features, but rather localized. Furthermore, the transects were not collected in a Lagrangian reference frame. Therefore, despite sampling the same water masses, they each observed different portions of the same water patches. This is even more so for the transects from Groups B and C, which were collected along different tracks. Based on this assumption, the errors associated with the averaged VT for each water mass presented in Figure 13 have been computed as

$$\delta VT = \sqrt{\sum_{tr}^{N} \left(\frac{\delta VT_{tr}}{N}\right)^2} \tag{A.6}$$

the sum in quadrature of each transect error divided by the number of transects included (N).

On the other end, if the estimates for the various transects were considered to be dependent, then the error δVT would have simply been computed as the simple average of the errors for each transect of the Group

$$\delta VT = \frac{1}{N}\sum_{tr}^{N} \delta VT_{tr} \tag{A.7}$$

Using equation A.7, the total errors for the three estimates presented in Figure 13 become 0.100, 0.029 and 0.012 Sv (for U, C+U and O' waters, respectively), corresponding to relative errors of 80, 40 and 56%.

Acknowledgments

The LATEX project was supported by the programs LEFE/IDAO and LEFE/CYBER of the INSU-Institut National des Sciences de l'Univers and by the Region PACA-Provence Alpes Côte d'Azur. F.N. acknowledges support from the FP7 Marie Curie Actions of the European Commission, via the Intra-European Fellowship (FP7-PEOPLE-IEF-2011), project "Lyapunov Analysis in the COaSTal Environment" (LACOSTE-299834). AVHRR data were supplied by Météo-France. The DT-INSU is thanked for the treatment of the thermosalinograph data. We thank the crews and technicians of the *R/V Le Suroît* and the *R/V Téthys II* and all the LATEX collaborators for their assistance at sea. The Latex10 data may be obtained from Francesco Nencioli (email: fne@pml.ac.uk)

References

Albérola, C., C. Millot, and J. Font (1995), On the seasonal and mesoscale variabilities of the Northern Current during the PRIMO-0 experiment in the western Mediterranean Sea, *Oceanol. Acta*, *18*(2), 163–192.

Allou, A., P. Forget, and J.-L. Devenon (2010), Submesoscale vortex structures at the entrance of the Gulf of Lions in the Northwestern Mediterranean Sea, *Continental Shelf Research*, *30*(7), 724 – 732, doi:http://dx.doi.org/10.1016/j.csr.2010.01.006.

Barbier, E. B., S. D. Hacker, C. Kennedy, E. W. Koch, A. C. Stier, and B. R. Silliman (2011), The value of estuarine and coastal ecosystem services, *Ecological Monographs*, *81*(2), 169–193, doi:10.1890/10-1510.1.

Barrier, N., A. A. Petrenko, and Y. Ourmières (2016), Strong intrusions of the Northern Mediterranean Current on the eastern Gulf of Lion: insights from in-situ observations and high resolution numerical modelling, *Ocean Dynamics*, *66*, 313–327, doi:10.1007/s10236-016-0921-7.

Bauer, J. E., and E. R. M. Druffel (1998), Ocean margins as a significant source of organic matter to the deep open ocean, *Nature*, *392*, 482–485, doi:10.1038/33122.

Biscaye, P. E., C. N. Flagg, and P. G. Falkowski (1994), The shelf edge exchange processes experiment, SEEP-II: an introduction to hypotheses, results and conclusions, *Deep Sea Res. II*, *41*(2-3), 231–252, doi:10.1016/0967-0645(94)90022-1.

Brink, K. H., and T. J. Cowles (1991), The Coastal Transition Zone program, *Journal of Geophysical Research: Oceans*, *96*(C8), 14,637–14,647, doi:10.1029/91JC01206.

Campbell, R., F. Diaz, Z. Hu, A. Doglioli, A. Petrenko, and I. Dekeyser (2013), Nutrients and plankton spatial distributions induced by a coastal eddy in the Gulf of Lion. Insights from a numerical model., *Prog. Oceanogr.*, *109*, 47–69, doi:10.1016/j.pocean.2012.09.005.

Canals, M., P. Puig, X. D. de Madron, S. Heussner, A. Palanques, and J. Fabres (2006), Flushing submarine canyons, *Nature*, *444*(7117), 354–357.

Castelao, R., O. Schofield, S. Glenn, R. Chant, and J. Kohut (2008), Cross-shelf transport of freshwater on the New Jersey shelf, *Journal of Geophysical Research: Oceans*, *113*, C07,017, doi:10.1029/2007JC004241.

Chereskin, T., M. Levine, A. Harding, and L. Regier (1989), Observations of near-inertial waves in acoustic Doppler current profiler measurements made during the mixed layer dynamics experiment, *J. Geophys. Res.*, *94*(C6), 8135–8145, doi:10.1029/JC094iC06p08135.

Csanady, G. (1982), *Circulation in the coastal ocean*, D.Reidel Publishing Company, Kluwer Group, Dordrech, Holland.

de Boyer Montégut, C., G. Madec, A. S. Fischer, A. Lazar, and D. Iudicone (2004), Mixed layer depth over the global ocean: An examination of profile data and a profile-based climatology, *Journal of Geophysical Research: Oceans*, *109*, doi: 10.1029/2004JC002378.

de Madron, X. D., L. Houpert, P. Puig, A. Sanchez Vidal, P. Testor, A. Bosse, C. Estournel, S. Somot, F. Bourrin, M. Bouin, M. Beauverger, L. Beguery, A. Calafat, M. Canals, C. Cassou, L. Coppola, D. Dausse, F. D'Ortenzio, J. Font, S. Heussner, S. Kunesch, D. Lefevre, H. Le Goff, J. Martín, L. Mortier, A. Palanques, and P. Raimbault (2013), Interaction of dense shelf water cascading and open-sea convection in the northwestern mediterranean during winter 2012, *Geophys. Res. Lett.*, *40*(7), 1379–1385, doi:10.1002/grl.50331.

Dinniman, M. S., J. M. Klinck, and W. O. Smith (2003), Cross-shelf exchange in a model of the Ross Sea circulation and biogeochemistry, *Deep Sea Research Part II: Topical Studies in Oceanography*, *50*(22–26), 3103–3120, doi:10.1016/j.dsr2.2003.07.011.

Doglioli, A. M., F. Nencioli, A. A. Petrenko, G. Rougier, J.-L. Fuda, and N. Grima (2013), A Software Package and Hardware Tools for In Situ Experiments in a Lagrangian Reference Frame, *J. Atmos. Oceanic Technol.*, *30*, 1940–1950, doi: 10.1175/JTECH-D-12-00183.1.

D'Ortenzio, F., and M. Ribera d'Alcalà (2009), On the trophic regimes of the Mediterranean Sea: a satellite analysis, *Biogeosciences*, *6*(2), 139–148, doi:10.5194/bg-6-139-2009.

d'Ovidio, F., V. Fernández, E. Hernández-García, and C. López (2004), Mixing structures in the Mediterranean Sea from finite-size Lyapunov exponents, *Geophys. Res. Lett.*, *31*, L17,203.

EEA (2010), 10 Messages for 2010 – Coastal ecosystems, *EEA Message 9*, European Environmental Agency, Copenhagen.

Estournel, C., X. Durrieu de Madron, P. Marsaleix, F. Auclair, C. Julliand, and R. Vehil (2003), Observation and modeling of the winter coastal oceanic circulation in the Gulf of Lion under wind conditions influenced by the continental orography (FETCH experiment), *Journal of Geophysical Research: Oceans*, *108*(C3), n/a–n/a, doi:10.1029/2001JC000825.

Fu, L.-L., and R. Ferrari (2008), Observing Oceanic Submesoscale Processes From Space, *Eos, Transactions American Geophysical Union*, *89*(48), 488–488, doi:

10.1029/2008EO480003.

Garcia Gorriz, E., J. Candela, and J. Font (2003), Near-inertial and tidal currents detected with a vessel-mounted acoustic Doppler current profiler in the western Mediterranean Sea, *J. Geophys. Res.*, *108*(C5), 3164.

Gattuso, J.-P., M. Frankignoulle, and R. Wollast (1998), Carbon and Carbonate Metabolism in Coastal Aquatic Ecosystems, *Annu. Rev. Ecol. Syst.*, *29*, pp. 405–434.

Grantham, B. A., F. Chan, K. J. Nielsen, D. S. Fox, J. A. Barth, A. Huyer, J. Lubchenco, and B. A. Menge (2004), Upwelling-driven nearshore hypoxia signals ecosystem and oceanographic changes in the northeast Pacific, *Nature*, *429*, 749–754, doi: 10.1038/nature02605.

Gustafsson, Ö., K. O. Buesseler, W. R. Geyer, S. B. Moran, and P. M. Gschwend (1998), An assessment of the relative importance of horizontal and vertical transport of particle-reactive chemicals in the coastal ocean, *Cont. Shelf Res.*, *18*(7), 805–829, doi:http://dx.doi.org/10.1016/S0278-4343(98)00015-6.

Haller, G., and G. Yuan (2000), Lagrangian coherent structures and mixing in two-dimensional turbulence, *Physica D: Nonlinear Phenomena*, *147*(3-4), 352 – 370, doi: 10.1016/S0167-2789(00)00142-1.

Haza, A. C., A. C. Poje, T. M. Özgökmen, and P. Martin (2008), Relative dispersion from a high-resolution coastal model of the Adriatic Sea, *Ocean Model.*, *22*(1¡80¿¡93¿2), 48 – 65, doi:10.1016/j.ocemod.2008.01.006.

Heslop, E. E., S. Ruiz, J. Allen, J. L. López Jurado, L. Renault, and J. Tintor (2012), Autonomous underwater gliders monitoring variability at ”choke points” in our ocean system: A case study in the Western Mediterranean Sea, *Geophys. Res. Lett.*, *39*(20), L20,604.

Hopkins, J., J. Sharples, and J. M. Huthnance (2012), On-shelf transport of slope water lenses within the seasonal pycnocline, *Geophys. Res. Lett.*, *39*(8), L08,604–.

Hu, Z., A. Petrenko, A. Doglioli, and I. Dekeyser (2011a), Study of a mesoscale anti-cyclonic eddy in the western part of the Gulf of Lion, *J. Mar. Sys.*, *88*(1), 3–11, doi: 10.1016/j.jmarsys.2011.02.008.

Hu, Z. Y., A. A. Doglioli, A. M. Petrenko, P. Marsaleix, and I. Dekeyser (2009), Numerical simulations of eddies in the Gulf of Lion, *Ocean Model.*, *28*(4), 203 – 208, doi:10.1016/j.ocemod.2009.02.004.

Hu, Z. Y., A. A. Petrenko, A. M. Doglioli, and I. Dekeyser (2011b), Numerical study of eddy generation in the western part of the Gulf of Lion, *J. Geophys. Res.*, *116*, C12,030, doi:10.1029/2011JC007074.

Huthnance, J. (1995), Circulation, exchange and water masses at the ocean margin: the role of physical processes at the shelf edge, *Prog. Oceanogr.*, *35*(4), 353–431, doi: 10.1016/0079-6611(95)00012-6.

Huthnance, J. M., H. M. Van Aken, M. White, E. Barton, B. L. Cann, E. Ferreira Coelho, E. Alvarez Fanjul, P. Miller, and J. Vitorino (2002), Ocean margin exchange-water flux estimates, *Journal of Marine Systems*, *32*(1-3), 107–137, doi:10.1016/S0924-7963(02)00034-9.

Huthnance, J. M., J. T. Holt, and S. L. Wakelin (2009), Deep ocean exchange with west-European shelf seas, *Ocean Science*, *5*(4), 621–634, doi:10.5194/os-5-621-2009.

Johnson, J., and P. Chapman (2011), Preface "Deep Ocean Exchange with the Shelf (DOES)", *Ocean Science*, *7*(1), 101–109, doi:10.5194/os-7-101-2011.

Juza, M., L. Renault, S. Ruiz, and J. Tintor (2013), Origin and pathways of winter intermediate water in the Northwestern Mediterranean sea using observations and numerical simulation, *Journal of Geophysical Research: Oceans*, *118*(12), 6621–6633, doi:10.1002/2013JC009231.

Kersalé, M., A. A. Petrenko, A. M. Doglioli, I. Dekeyser, and F. Nencioli (2013), Physical characteristics and dynamics of the coastal Latex09 Eddy derived from in situ data and numerical modeling, *J. Geophys. Res.-Oceans*, *118*, 1–11, doi:10.1029/2012JC008229.

Klein, P., and Hua, B. L. (1988), Mesoscale heterogeneity of the wind-driven mixed layer: Influence of a quasigeostrophic flow, *Journal of Marine Research*, *46*(3), 495–525, doi:10.1357/002224088785113568.

Klymak, J. M., R. K. Shearman, J. Gula, C. M. Lee, E. A. D'Asaro, L. N. Thomas, R. R. Harcourt, A. Y. Shcherbina, M. A. Sundermeyer, J. Molemaker, and J. C. McWilliams (2016), Submesoscale streamers exchange water on the north wall of the Gulf Stream, *Geophysical Research Letters*, pp. n/a–n/a, doi:10.1002/2015GL067152, 2015GL067152.

Kirincich, A. R., and J. A. Barth (2009), Time-Varying Across-Shelf Ekman Transport and Vertical Eddy Viscosity on the Inner Shelf, *J. Phys. Oceanogr.*, *39*(3), 602–620, doi:10.1175/2008JPO3969.1.

Lehahn, Y., F. d'Ovidio, M. Levy, and E. Heifetz (2007), Stirring of the northeast Atlantic spring bloom: A Lagrangian analysis based on multisatellite data, *J. Geophys. Res.*, *112*(C8), C08,005.

Liu, K.-K., L. Atkinson, R. Quiñones, and L. Talaue McManus (2010), *Carbon and nutrient fluxes in continental margins: a global synthesis*, Springer-Verlag, Berlin Heildeberg.

Liu, Y., R. H. Weisberg, S. Vignudelli, and G. T. Mitchum (2014), Evaluation of altimetry-derived surface current products using Lagrangian drifter trajectories in the eastern Gulf of Mexico, *Journal of Geophysical Research: Oceans*, pp. n/a–n/a, doi: 10.1002/2013JC009710.

Lumpkin, R., and S. L. Garzoli (2005), Near-surface circulation in the Tropical Atlantic Ocean, *Deep Sea Research Part I: Oceanographic Research Papers*, *52*(3), 495 – 518, doi:http://dx.doi.org/10.1016/j.dsr.2004.09.001.

Malanotte Rizzoli, P., V. Artale, G. L. Borzelli Eusebi, S. Brenner, A. Crise, M. Gacic, N. Kress, S. Marullo, M. Ribera d'Alcalà, S. Sofianos, T. Tanhua, A. Theocharis, M. Alvarez, Y. Ashkenazy, A. Bergamasco, V. Cardin, S. Carniel, G. Civitarese, F. D'Ortenzio, J. Font, E. Garcia Ladona, J. M. Garcia Lafuente, A. Gogou, M. Gregoire, D. Hainbucher, H. Kontoyannis, V. Kovacevic, E. Kraskapoulou, G. Kroskos, A. Incarbona, M. G. Mazzocchi, M. Orlic, E. Ozsoy, A. Pascual, P.-M. Poulain, W. Roether, A. Rubino, K. Schroeder, J. Siokou Frangou, E. Souvermezoglou, M. Sprovieri, J. Tintoré, and G. Triantafyllou (2014), Physical forcing and physical/biochemical variability of the Mediterranean Sea: a review of unresolved issues and directions for future research, *Ocean Science*, *10*(3), 281–322, doi:10.5194/os-10-281-2014.

Matsuno, T., J.-S. Lee, and S. Yanao (2009), The Kuroshio exchange with the South and East China Seas, *Ocean Science*, *5*(3), 303–312, doi:10.5194/os-5-303-2009.

Millot, C. (1979), Wind induced upwellings in the Gulf of Lions, *Oceanol. Acta*, *2*, 261–274.

Millot, C. (1990), The Gulf of Lions' hydrodynamics, *Cont. Shelf Res.*, *10*, 885–894, doi:10.1016/0278-4343(90)90065-T.

Millot, C., and M. Crépon (1981), Inertial Oscillations on the Continental Shelf of the Gulf of Lions – Observations and Theory, *J. Phys. Oceanogr.*, *11*(5), 639–657.

Nagai, T., N. Gruber, H. Frenzel, Z. Lachkar, J. C. McWilliams, and G.-K. Plattner (2015), Dominant role of eddies and filaments in the offshore transport of carbon and nutrients in the California Current System, *Journal of Geophysical Research: Oceans*, pp. n/a–n/a, doi:10.1002/2015JC010889.

Nencioli, F., F. d'Ovidio, A. M. Doglioli, and A. A. Petrenko (2011), Surface coastal circulation patterns by in-situ detection of Lagrangian coherent structures, *Geophys. Res. Lett.*, *38*(17), L17,604, doi:10.1029/2011GL048815.

Nencioli, F., F. d'Ovidio, A. M. Doglioli, and A. A. Petrenko (2013), In situ estimates of submesoscale horizontal eddy diffusivity across an ocean front, *Journal of Geophysical Research: Oceans*, *118*(12), 7066–7080, doi:10.1002/2013JC009252.

Ohlmann, J. C., P. P. Niiler, C. A. Fox, and R. R. Leben (2001), Eddy energy and shelf interactions in the Gulf of Mexico, *Journal of Geophysical Research: Oceans*, *106*(C2), 2605–2620, doi:10.1029/1999JC000162.

Olascoaga, M. J., I. I. Rypina, M. G. Brown, F. J. Beron-Vera, H. Kocak, L. E. Brand, G. R. Halliwell, and L. K. Shay (2006), Persistent transport barrier on the West Florida Shelf, *Geophys. Res. Lett.*, *33*(22), doi:10.1029/2006GL027800.

Özgökmen, T. M., A. C. Poje, P. F. Fischer, and A. C. Haza (2011), Large eddy simulations of mixed layer instabilities and sampling strategies, *Ocean Model.*, *39*(3-4), 311 – 331, doi:10.1016/j.ocemod.2011.05.006.

Petrenko, A. (2003), Variability of circulation features in the gulf of lion NW Mediterranean Sea. Importance of inertial currents, *Oceanol. Acta*, *26*(4), 323–338, doi: 10.1016/S0399-1784(03)00038-0.

Petrenko, A., Y. Leredde, and P. Marsaleix (2005), Circulation in a stratified and wind-forced Gulf of Lions, NW Mediterranean Sea: in situ and modeling data, *Cont. Shelf Res.*, *25*, 7–27, doi:10.1016/j.csr.2004.09.004.

Petrenko, A. A., C. Dufau, and C. Estournel (2008), Barotropic eastward currents in the western Gulf of Lion, northwestern Mediterranean Sea, during stratified conditions, *J. Mar. Sys.*, *74*(1-2), 406–428, doi:10.1016/j.jmarsys.2008.03.004.

Piola, A. R., N. Martínez Avellaneda, R. A. Guerrero, F. P. Jardón, E. D. Palma, and S. I. Romero (2010), Malvinas-slope water intrusions on the northern Patagonia continental shelf, *Ocean Science*, *6*(1), 345–359, doi:10.5194/os-6-345-2010.

Poulain, P.-M., M. Menna, and E. Mauri (2012), Surface Geostrophic Circulation of the Mediterranean Sea Derived from Drifter and Satellite Altimeter Data, *J. Phys. Oceanogr.*, *42*(6), 973–990, doi:10.1175/JPO-D-11-0159.1.

Ralph, E. A., and P. P. Niiler (1999), Wind-Driven Currents in the Tropical Pacific, *J. Phys. Oceanogr.*, *29*(9), 2121–2129, doi:10.1175/1520-0485(1999)029¡2121:WDCITT¿2.0.CO;2.

Ross, O. N., M. Fraysse, C. Pinazo, and I. Pairaud (2016), Impact of an intrusion by the Northern Current on the biogeochemistry in the eastern Gulf of Lion, NW Mediterranean, *Estuarine, Coastal and Shelf Science*, *170*, 1–9, doi:10.1016/j.ecss.2015.12.022.

Roughan, M., N. Garfield, J. Largier, E. Dever, C. Dorman, D. Peterson, and J. Dorman (2006), Transport and retention in an upwelling region: The role of across-shelf structure, *Deep Sea Res. II*, *53*(25–26), 2931–2955, doi:10.1016/j.dsr2.2006.07.015.

Rubio, A., V. Taillandier, and P. Garreau (2009), Reconstruction of the Mediterranean northern current variability and associated cross-shelf transport in the Gulf of Lions from satellite-tracked drifters and model outputs, *J. Mar. Sys.*, *78*(Sp. Iss. SI Suppl. S), S63–S78, doi:10.1016/j.jmarsys.2009.01.011.

Sammari, C., C. Millot, and L. Prieur (1995), Aspects of the seasonal and mesoscale variabilities of the Northern Current in the western Mediterranean Sea inferred from the PROLIG-2 and PROS-6 experiments, *Deep-Sea Res. I*, *42*(6), 893–917, doi: 10.1016/0967-0637(95)00031-Z.

Schaeffer, A., P. Garreau, A. Molcard, P. Frauni, and Y. Seity (2011), Influence of high-resolution wind forcing on hydrodynamic modeling of the Gulf of Lions, *Ocean Dynamics*, *61*(11), 1823–1844, doi:10.1007/s10236-011-0442-3.

Shapiro, G. I., S. V. Stanichny, and R. R. Stanychna (2010), Anatomy of shelf-deep sea exchanges by a mesoscale eddy in the North West Black Sea as derived from remotely sensed data, *Remote Sensing of Environment*, *114*(4), 867 – 875, doi: http://dx.doi.org/10.1016/j.rse.2009.11.020.

Shcherbina, A., E. A. D'Asaro, C. M. Lee, J. M. Klymak, M. J. Molemaker, and J. C. McWilliams (2013), Statistics of vertical vorticity, divergence, and strain in a developed submesoscale turbulence field, *Geophysical Research Letters*, pp. n/a–n/a, doi: 10.1002/grl.50919.

Thomas, L. N., A. Tandon, and A. Mahadevan (2008), Submesoscale processes and dynamics, in *Ocean Modeling in an Eddying Regime*, *Geophysical Monograph Series*, vol. 177, pp. 17–38, AGU, Washington, DC, doi:10.1029/GM177.

UNESCO (2011), A Blueprint for Ocean and Coastal Sustainability, *Report*, IOC/UNESCO, IMO, FAO, UNDP, Paris, pp. 42.

Weller, R. A. (1982), The Relation of Near-Inertial Motions Observed in the Mixed layer During the JASIN (1978) Experiment to the Local Wind Stress and to the Quasi-Geostrophic Flow Field, *Journal of Physical Oceanography*, *12*(10), 1122–1136, doi:

10.1175/1520-0485(1982)012¡1122:TRONIM¿2.0.CO;2.

Zhou, F., G. Shapiro, and F. Wobus (2014), Cross-shelf exchange in the northwestern Black Sea, *Journal of Geophysical Research: Oceans*, *119*(4), 2143–2164, doi: 10.1002/2013JC009484.

Supporting Information for "Diagnosing cross-shelf transport along an ocean front: an observational case study in the Gulf of Lion"

F. Nencioli,[1,2] A. A. Petrenko,[2] A. M. Doglioli,[2]

Contents of this file

1. Figures 1 to 8

Corresponding author: F. Nencioli

Tel: +44 (0)1752 633427

Email: fne@pml.ac.uk

[1]Plymouth Marine Laboratory, Prospect Place, The Hoe, Plymouth, Devon, PL1 3DH, UK

[2]Aix Marseille Université, CNRS, Université de Toulon, IRD, MIO UM 110, 13288, Marseille, France

Introduction

This document contains material to support some of the hypotheses and results of the paper. In particular, it provides additional information on:

- quantification of the average MLD (figure 1)
- vertical variations of velocity within the MLD (figure 2)
- Ekman current estimates (figures 3 and 4)
- density cross-front sections (figure 5)
- quantification of the vorticity Rossby number (figure 6)
- histogram of TS observations (figure 7)
- along-transect distribution of $(\delta VT_{tr})_i$ (figure 8)

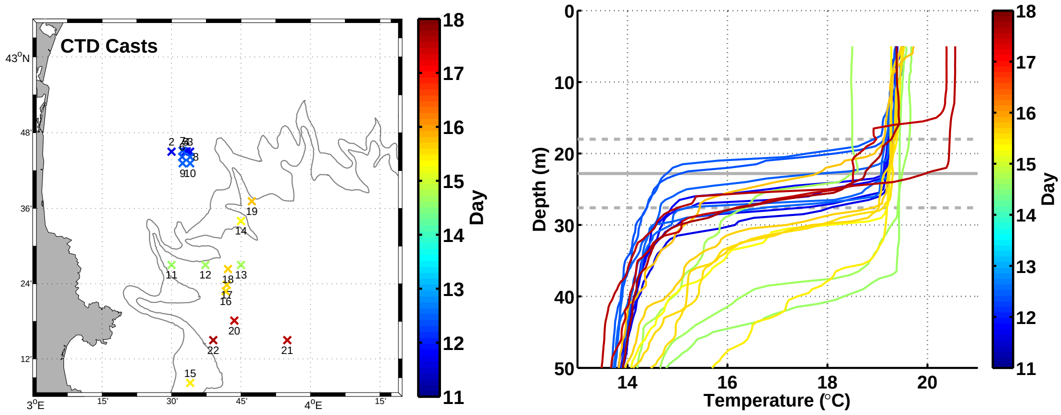

Figure 1. (*Left panel*) Position of the 21 CTD casts (numbered 2 to 22) collected during Latex10 between 11 to 22 September. (*Right panel*) Corresponding vertical profiles of temperature. In both panels position and profiles are color coded according to the day they were collected. The range of the colorbar has been adjusted to 18 September, day when the last CTD profile was collected. The solid grey line marks the average MLD ($\Delta z = 22.8$ m). The dashed lines mark the one standard deviation interval $\Delta z \pm \delta z$ ($\delta z = 4.8$ m). The relative error $\delta z/\Delta z$ used in equation A1 is 21%. Similar analysis using a temperature difference of 0.5°C showed analogous results with $\Delta z = 25.6$, $\delta z = 5.2$ and $\delta z/\Delta z = 20\%$.

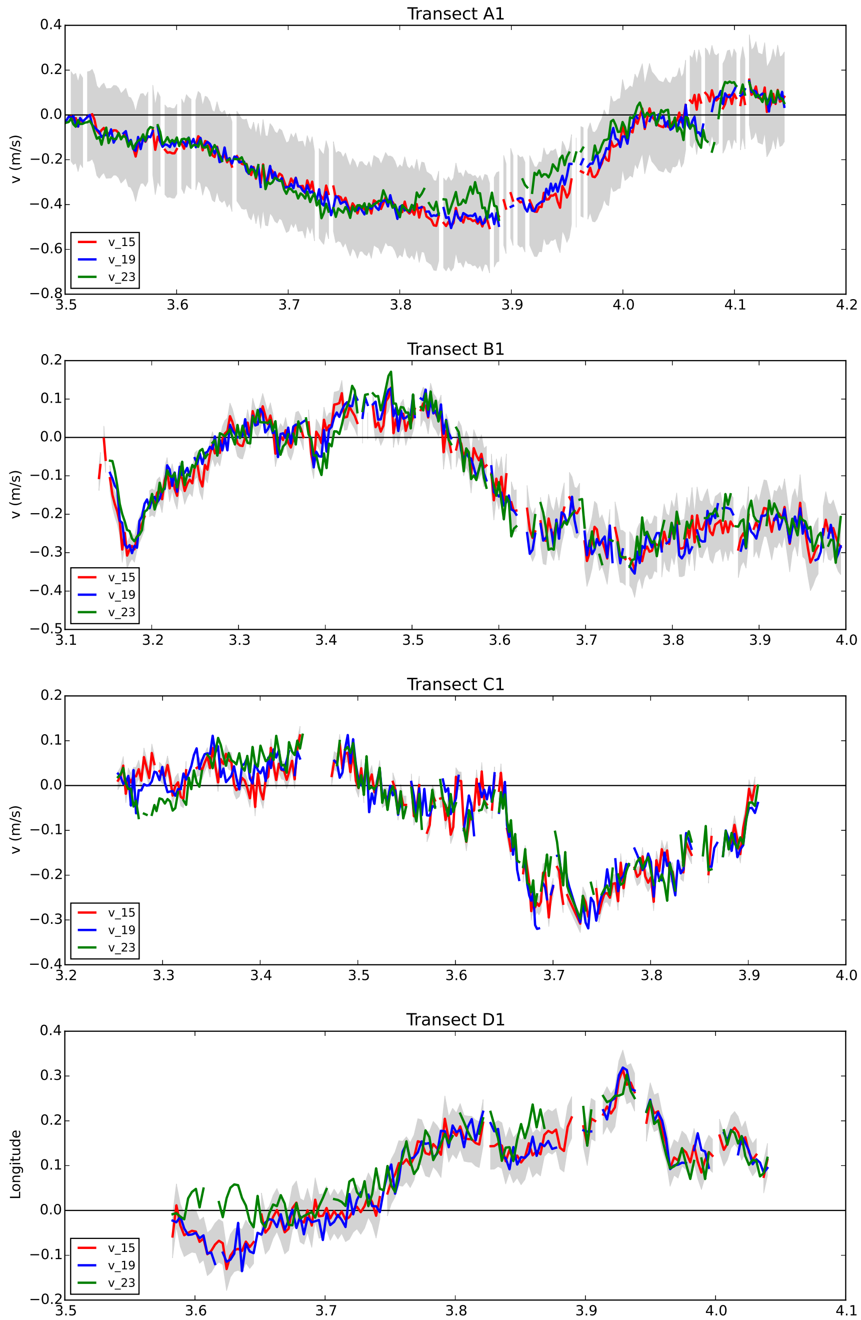

Figure 2. Comparison between $v_{tr,15}$ (red), $v_{tr,19}$ (blue), $v_{tr,23}$ (green) and $v_{tr,15} \pm \delta v$ (shaded gray) for the first transects of each group. Vertical variations of velocity within the mixed layer are usally within the instrument precision and smaller than the uncertainities associated with NIO corrections. The largest differences are observed at 23 m depth, the base of the MLD. Averaged over the transect length, the velocity differences result in negligible net contributions.

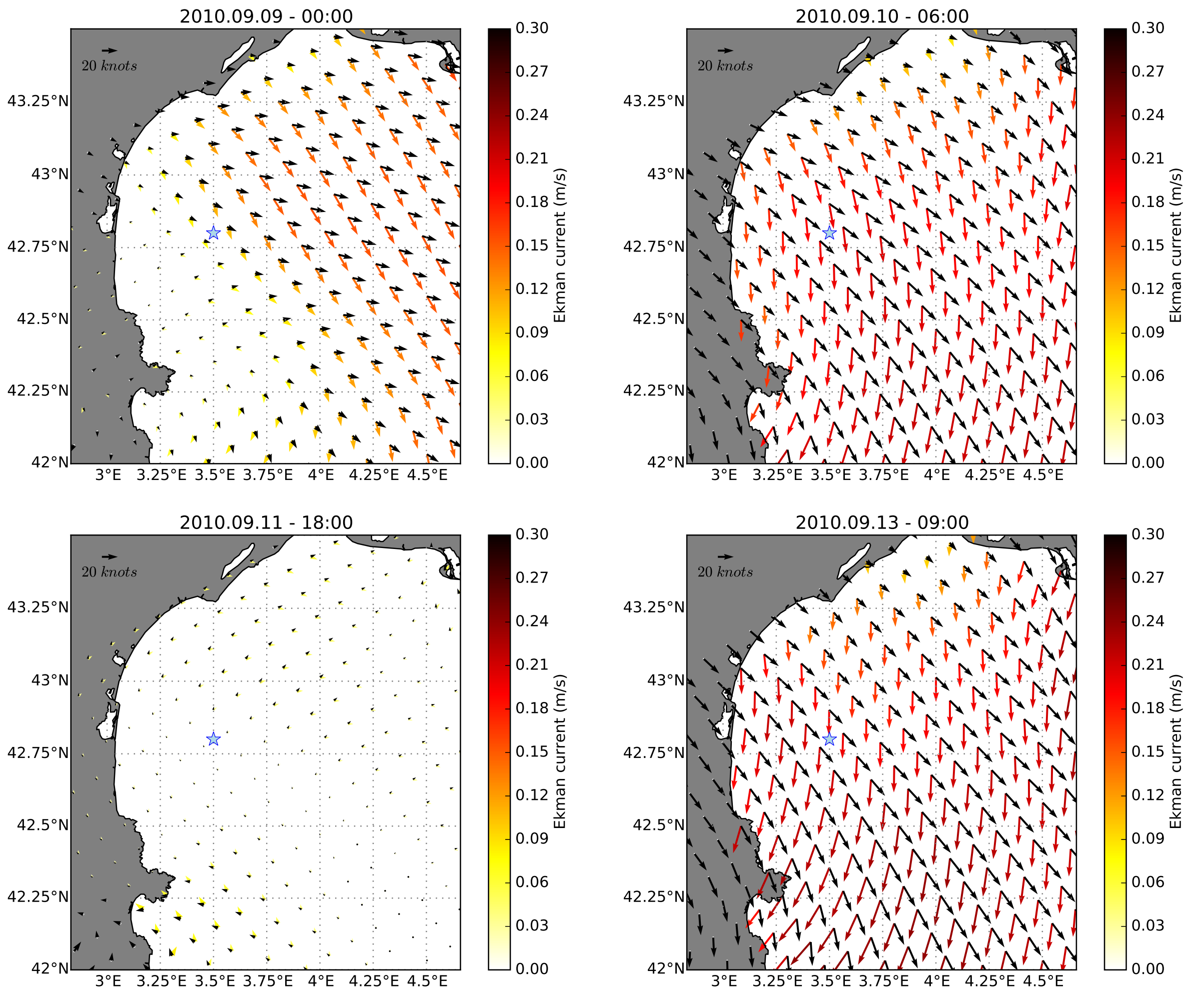

Figure 3. Successive maps of wind (black arrows) and resulting Ekman currents (colored arrows). The two wind events between 9 and 15 September generated predominatly southward currents between 0.20 and 0.25 m s^{-1}. The blue star marks the location of Lyap01 deployment, at which the time series in figure 4 has been derived.

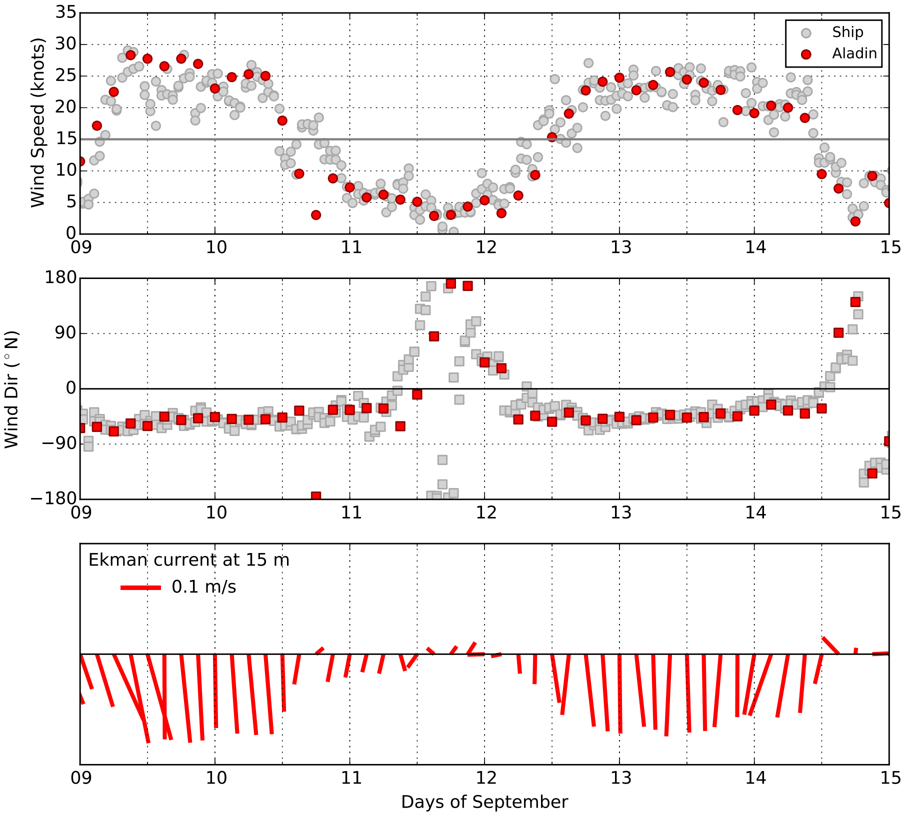

Figure 4. (Top and middle) Comparison between ship-recorded (gray) and ALADIN (red) wind velocity and direction at the location of the Lyap01 deployment (see figure 3) from 9 to 15 September, showing good agreement between the two. (Bottom) Resulting wind-induced currents. The current direction is consistent with the observed Lyap01 trajectories, and its magnitude of the same order as the $\mathbf{u}_{NIO}$ reconstructed from the drifters.

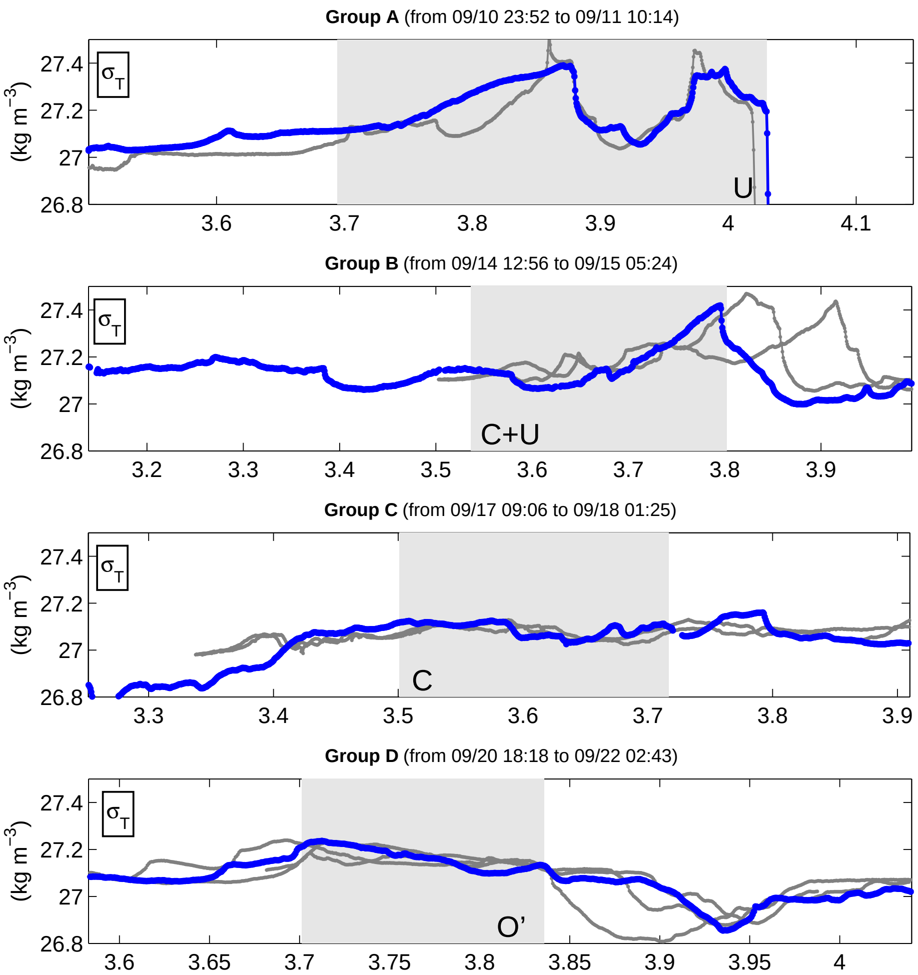

Figure 5. Density sections across the front for groups A to D. As in Figures 8 to 11, the first transect of each group is shown in color, while the others are in gray. The gray area marks the portion of each transect along which the outflowing and inflowing water masses defined in Section 3.2 have been identified. The front is mostly compensated when it results from C and O waters only, as in Groups C and D. On the other hand, when U waters are present as in Groups A and B, the transitions between the different water masses are also characterized by cross-front density gradients.

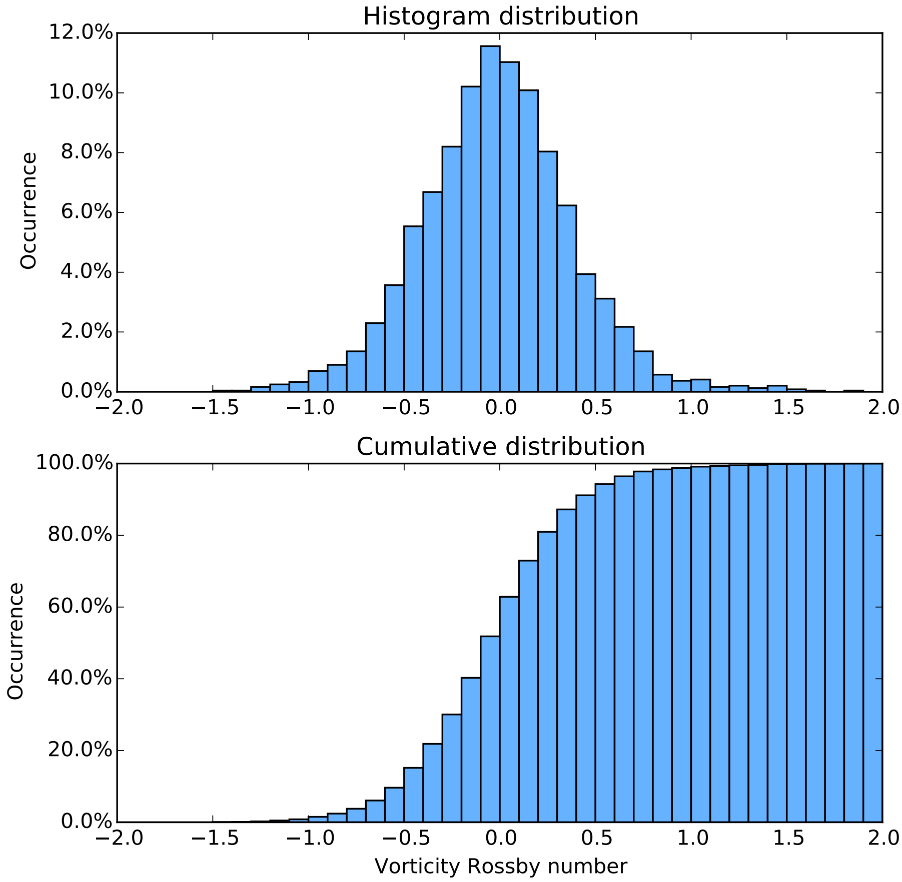

Figure 6. Histogram and cumulative distribution of the vorticity Rossby number ($R_o = \zeta/f$) from the observations along all group A to D transects. The dominant values are $< \mathcal{O}(1)$, indicating that the front was mainly associated with geostrophic (i.e. mesoscale) dynamics.

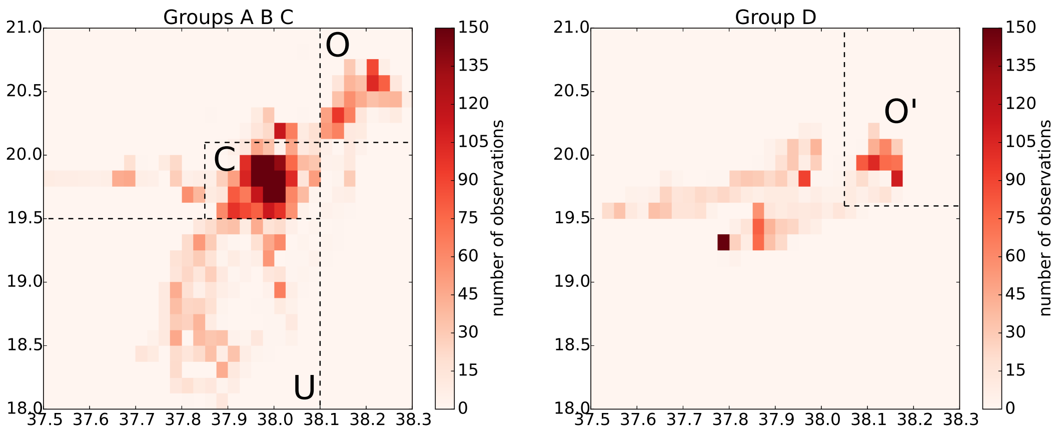

Figure 7. Histograms of TS observations for Groups A to C (left) and for Group D (right). The observations are binned every 0.025 psu and 0.125°C, respectively. As in Figure 4 in the text, the dashed lines mark the identified SST and SSS thresholds separating the clusters of observations associated with U, C and O waters. Group D is shown separately due to the modifications in the surface TS signatures following intense wind and sgtrong rain conditions in the western part of the GoL between 18 and 19 September (see text for more details).

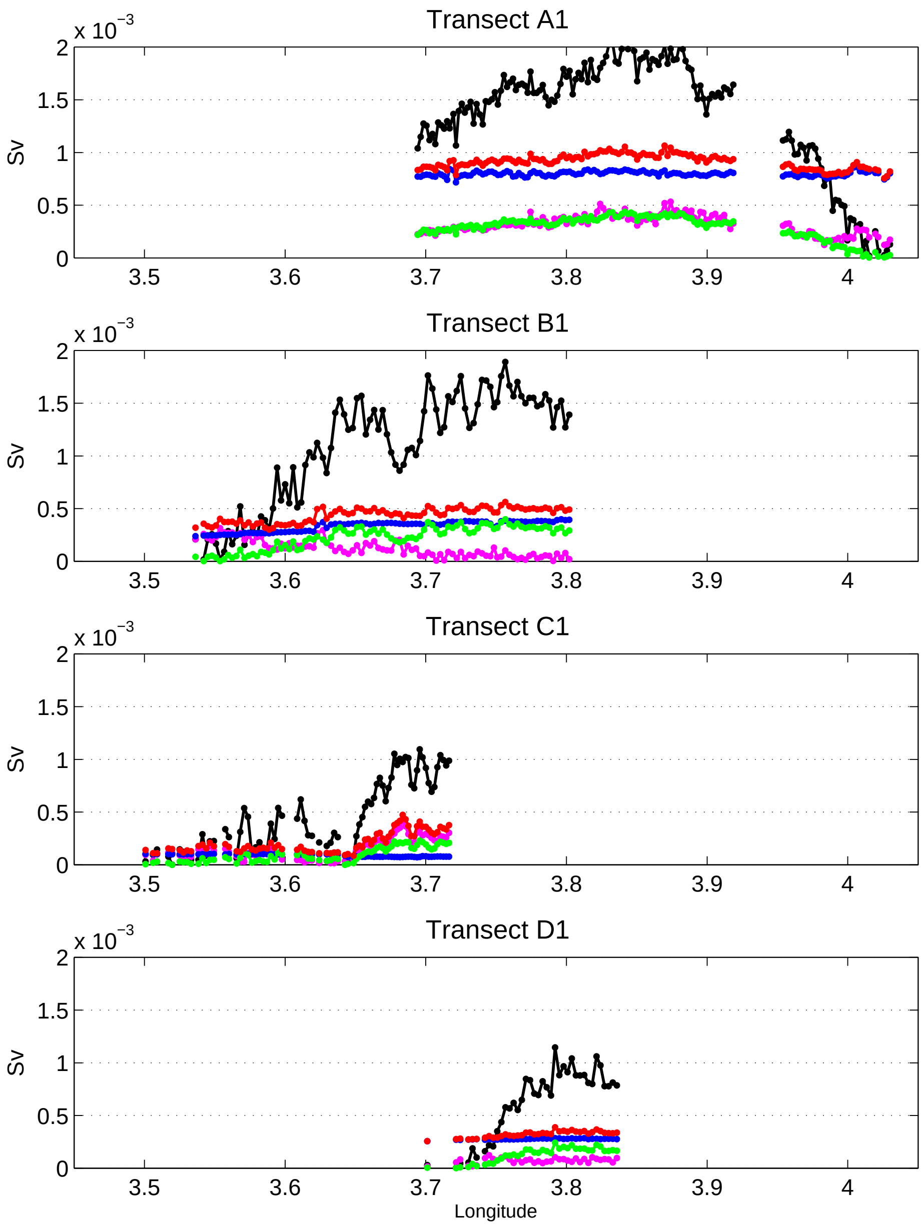

Figure 8. Distribution of the absolute values of $(VT_{tr})_i$ (Equation 3) and the associated uncertainties along the first transects of each group. Black line: $(VT_{tr})_i$; red line: $(\delta VT_{tr})_i$ (equation A1); blue line $(\delta VT_{tr})_i$ with the contribution from the relative velocity error $(\delta v_{tr}/\tilde{v}_{tr,15})$ only; green line $(\delta VT_{tr})_i$ with the contribution of the relative MLD error $(\delta z/\Delta z)$ only; magenta line $(\delta VT_{tr})_i$ with the contribution of the relative direction error only (last term in equation A2).